Chloride partitioning and solubility in hydrous phonolites from Erebus volcano: A contribution towards a multi-component degassing model

Marina Alletti, Alain Burgisser, Bruno Scaillet, Clive Oppenheimer

To cite this version:

Marina Alletti, Alain Burgisser, Bruno Scaillet, Clive Oppenheimer. Chloride partitioning and solubility in hydrous phonolites from Erebus volcano: A contribution towards a multi-component degassing model. GeoResJ, 2014, 3-4, pp.27-45. 10.1016/j.grj.2014.09.003 . insu-01092380

HAL Id: insu-01092380
https://insu.hal.science/insu-01092380

Submitted on 19 Mar 2015

GeoResJ 3-4 (2014) 27–45

Contents lists available at ScienceDirect

GeoResJ

journal homepage: www.elsevier.com/locate/GRJ

Chloride partitioning and solubility in hydrous phonolites from Erebus volcano: A contribution towards a multi-component degassing model

Marina Alletti [a,b], Alain Burgisser [c,d,*], Bruno Scaillet [a,b], Clive Oppenheimer [e]

[a] CNRS, ISTO, F-45071 Orléans, France
[b] Université d'Orléans, ISTO, F-45071 Orléans, France
[c] CNRS, ISTerre, F-73376 Le Bourget du Lac, France
[d] Université de Savoie, ISTerre, F-73376 Le Bourget du Lac, France
[e] Department of Geography, University of Cambridge, Downing Place, Cambridge CB2 3EN, UK

ARTICLE INFO

Article history:
Received 21 April 2014
Revised 26 September 2014
Accepted 26 September 2014
Available online 21 October 2014

Keywords:
Chlorine
Volcanic gas
Solubility
Lava lake
Phonolite

ABSTRACT

We present results from a series of experiments on the partitioning of chlorine between a hydrous fluid phase and a phonolitic melt that we then use to model specific aspects of volcanic degassing. Experiments were performed from 250 to 10 MPa on a phonolite from Erebus lava lake, Antarctica, at 1000 °C near the QFM solid buffer. Only one of 48 experimental samples shows coexistence of low-density vapour and high-density brine in the fluid phase while 35 samples are unambiguously in the vapour field. Large uncertainties in the H_2O–NaCl phase diagram at the *P*–*T* considered do not allow us to assign reliable phase behaviour to the remaining samples. We select a vapour-dominated subset of our dataset to establish an empirical HCl solubility law valid at low pressures and salinities. This law is incorporated into a thermodynamical model of degassing, which we use to compute equilibrium temperatures from gas measurements made at Erebus in 2010. The quiescent lake activity features cyclic temperature variations between 1000 and 1050 °C, which is consistent with thermal convection within the shallow plumbing system. Backward tracking of representative gas compositions and temperatures shows the evolution with pressure of the molar ratio of SO_2/HCl in the gas, a quantity that is often measured in volcanic plumes. Model outputs suggest that this ratio can vary by up to an order of magnitude when the pressure changes from atmospheric to 100 MPa, depending on degassing style (coupled vs. decoupled ascent of gas and melt).

1. Introduction

Erebus volcano (Antarctica) hosts one of the few persistent active lava lakes on Earth, and the only one of phonolite composition. Despite its remoteness, the lake is closely studied and its gas emissions have been measured during successive austral summer field seasons since 2004 using Fourier transform infrared (FTIR) spectroscopic methods [37,40,41,5,9]. Time series analyses of the volcanic gas chemistry show systematic smooth variations when the lava lake convects and emits gases in a quiescent fashion [40] and sudden compositional shifts when large gas bubbles explosively disrupt the lake surface [41]. Melt inclusions in anorthoclase and pyroxene crystals hosted in Erebus phonolite have H_2O concentrations similar to or lower than those of halogens (i.e., Cl and F), which indicates extensive degassing of the magma [19]. This begs the question of the depth at which the volcanic gases originate at Erebus. Oppenheimer and Kyle [37] presented the first study proposing a link between gas composition and varying source depths. They used degassing models that neglect the multi-component nature of the fluid phase, and that did not include experimentally-determined solubilities of Na-phonolitic melts. Later, Oppenheimer et al. [41] used the multicomponent thermodynamical model of Papale et al. [42], which was calibrated with an experimental database on melt compositions approaching but distinct from that of Erebus phonolite. They suggested that the degassing at Erebus originates from depths spanning from mantle to surface. Recently, Burgisser et al. [9] included new H_2O solubility data for Erebus in their multicomponent thermodynamical model, D-Compress, which they used to find equilibrium temperatures of a few representative gas compositions. They concluded that the quiescent gas last equilibrated at ~1080 °C, whereas the gas coming from bubble bursts cools down of a few hundred degrees during the explosions. Taking these equilibrium gas compositions at atmospheric pressure and recompressing them to higher pressures

---

* Corresponding author at: CNRS, ISTerre, F-73376 Le Bourget du Lac, France. Tel.: +33 479 758 780; fax: +33 479 758 742.

E-mail address: alain.burgisser@univ-savoie.fr (A. Burgisser).

http://dx.doi.org/10.1016/j.grj.2014.09.003
2214-2428/

either in contact with a phonolitic melt, or as pure gas, they calculated how the respective volatile compositions of gas and melt change with depth. These simulations suggested that the gas compositional variations can be explained by very shallow processes, although deeper volatile sources cannot be excluded.

None of these recent works, however, considered the role of chlorinated species. This partly stems from the lack of both suitable experimental data and an adequate modelling framework. Chlorine solubility in silicate melts is greatly affected, like most volatiles, by pressure and magma composition [11]. Several studies have been made on the solubility of major volatile elements in phonolitic melts. Water solubility in Na-rich phonolite has successively been addressed by Carroll and Blank [12], Larsen and Gardner [28], and Schmidt and Behrens [48]. The specific case of water solubility in the Na-phonolite of Erebus was presented in Burgisser et al. [9] for pressures between 10 and 250 MPa. Iacono-Marziano et al. [25] performed equilibrium experiments for water solubility in K-phonolite over a similar pressure range. Morizet et al. [32] studied CO_2 solubility and speciation in a haplo-phonolite at deep crust/mantle conditions. Signorelli and Carroll [54] performed experiments of chlorine solubility and fluid/melt partitioning in a hydrous Na-phonolitic melt between 50 and 250 MPa. Chevychelov et al. [13] performed experiments of Cl and F partitioning between a hydrous fluid and a phonolitic melt of Mount Vesuvius at 200 MPa, and Webster et al. [68] reported on experiments with Cl, S, and H_2O at that same pressure for phonolitic and trachytic melts. This short inventory reveals a lack of data on Cl solubility at low-pressure (<50 MPa) in Na-phonolite melts such as that of Erebus. This gap in the pressure range 0.1–50 MPa is present in many experimental studies addressing Cl behaviour in other magmatic compositions [50]. Filling this gap would be of great help to understand chlorine variations in the Erebus gas plume and elsewhere.

Most efforts to model Cl degassing have used the concept of partition coefficients (e.g, [62,23,63]. While enabling investigation of a wide range of pressures and exploration of important aspects of volcanic degassing, this approach is impractical when dealing with the effects of the multicomponent nature of magmatic volatiles on degassing. More complete descriptions of Cl behaviour, however, are hindered by the existence of an immiscibility domain in the fluid phase between a low density, H_2O-dominated vapour and a dense, Na(K, Fe, Ca)Cl-rich brine (e.g., [3,17,50,43]. In alkaline melts such as the Erebus phonolite, this observed immiscibility [54] is modified in complex ways by the abundance of Na and K in the melt, which partition with fluid phase and influence Cl partitioning (e.g., [66,69].

With the overall goal to increase our knowledge of the magmatic degassing paths at Erebus in the fugacity-volatile composition space, we performed experiments on the partitioning of Cl between a hydrous fluid phase and a phonolitic melt at 1000 °C and log $f_{O2} \sim$ QFM over a range of pressure from 10 to 250 MPa. After depicting the chloride saturation in the melt and the composition of the fluid phase from our experiments, we select a subset of data amenable to the modelling of Cl solubility at low pressures ($\leqslant$100 MPa). We include the resulting solubility law into the thermodynamic multicomponent model D-Compress [7,8,9]. We also update the method of solution to calculate equilibrium temperatures from measured gas ratios. We use gas composition measurements made at Erebus on emissions from the lava lake as input data for the updated thermodynamical model so as to analyse the evolution of gas temperature with time. This analysis yields a comprehensive assessment of daily variations in gas composition and temperature. Finally, we perform recompression runs with D-Compress using representative gas compositions as inputs to back-track the evolution of both dissolved and exsolved chlorine as a function of pressure.

2. Experimental method, analytical techniques, and modelling approach

2.1. Starting material

A natural Na-rich phonolite bomb ejected from the lava lake of Mount Erebus (ERE 13-29 Dec 05) was used as the experimental starting composition. Such phonolite bombs contain large phenocrysts of anorthoclase up to 10 cm in length. A previous study [9] showed that using either the whole rock, or the residue after removing the largest crystals (longer than 0.5 cm) before the fusion at 1400 °C does not substantially affect the bulk composition of the resulting starting glass or the solubility of water. For this study, we crushed and ground the bulk phonolite sample in an agate mortar before fusing it at 1400 °C for 2 h in a platinum crucible in a 1-atm furnace. This operation was repeated twice and, at the end of each fusion, the melt was quenched in a water bath. In this way any naturally present volatiles (H_2O and CO_2) were removed. The highly oxidizing conditions (open atmosphere) minimize the amount of Fe loss to the crucible [34]. Chips of this glass were mounted in epoxy for compositional analyses (Table 1) by Electron MicroProbe Analyser (EMPA), and the rest was ground and stored in a drying oven at 120 °C.

2.2. Experimental procedure

Experiments were performed in a rapid-quench Internally Heated Pressure Vessel (IHPV), working vertically, at 1000 °C and in a pressure range of 250–10 MPa. A mixture of Ar–H_2 obtained by sequential loading of the two gases at room temperature [16] was used as the pressure medium in order to work at an oxygen fugacity between QFM and QFM+1 [26]. Since H_2 sequestration by vessel walls may happen over run duration (68–89 h, Table 2), experimental f_{H2} was monitored by CoPdO sensors.

Partitioning experiments consisted of preparing initially hydrous saline solutions at six different chloride concentrations, from 0.6 to 19 wt.%. KCl and NaCl were added to distilled water in order to make solutions with a molar ratio Na/K of ~2.4 ± 0.1, near that of the starting material. Au capsules were filled with about 50 mg of glass powder and the saline solutions so that the system remained saturated with respect to H_2O at each experimental pressure. Capsules were always loaded so that the mass ratio between the fluid phase and the glass was equal to or lower than 0.1, which avoids significant silicate dissolution into fluid during the experiments. One CoPdO sensor was loaded for each run in order to monitor the prevailing f_{H2}. Each sensor was prepared with two pellets of CoPd metal mixtures (each with different Co/Pd ratio) plus CoO, sealed in Au capsules with excess H_2O and embedded in ZrO_2 [59]. Sensors were placed with the six other phonolite-filled capsules in the sample holder during each experiment. The

Table 1
Starting material composition. Oxide contents are in wt.% and values in parenthesis are standard errors.

Oxide	wt.%
SiO_2	55.54 (0.30)
TiO_2	1.12 (0.04)
Al_2O_3	19.26 (0.10)
FeO	5.42 (0.09)
MnO	0.25 (0.06)
MgO	1.04 (0.03)
CaO	2.52 (0.06)
Na_2O	7.74 (0.12)
K_2O	4.82 (0.10)
P_2O_5	0.49 (0.04)
Cl	0.09 (0.01)
Total	98.30

Table 2
Run conditions, volatile contents, and redox state of experiments. Symbols are listed in the Methods section.

Run conditions		Sample	W_{gl} (mg)	$^iW_{H2O}$ (mg)	$^iW_{alk}$ (mg)	C^m_{Cl} (wt.%)	C^m_{H2O} (wt.%)	W^f_{Cl}[a] (mg)	W^f_{H2O}[a] (mg)	ΔQFM
P (MPa)	250	ERE-2-A	51.70	6.73	0.07	0.14	7.18	0.0142 (0.019)	2.73 (0.40)	0.36
$^iC^m_{Cl}$ (wt.%)	0.10	ERE-2-1	52.30	6.68	0.22	0.26	6.90	0.0324 (0.021)	2.79 (0.39)	0.36
Duration (h)	67.5	ERE-2-2	50.10	6.63	0.37	0.37	7.23	0.0586 (0.023)	2.71 (0.39)	0.35
		ERE-2-3	52.00	6.66	0.76	0.60	6.99	0.139 (0.031)	2.71 (0.40)	0.34
		ERE-2-4	50.90	6.67	1.59	0.77	6.97	0.521 (0.039)	2.80 (0.39)	0.28
		ERE-2-5	52.00	6.59	3.42	0.89	7.35	1.47 (0.055)	2.40 (0.42)	0.13
P (MPa)	200	ERE-1-A	50.50	5.44	0.06	0.14	5.95	0.0050 (0.019)	2.24 (0.32)	0.60
$^iC^m_{Cl}$ (wt.%)	0.09	ERE-1-1	50.10	5.42	0.18	0.25	5.95	0.0145 (0.021)	2.24 (0.32)	0.59
Duration (h)	75	ERE-1-2	50.50	5.50	0.31	0.36	5.62	0.0260 (0.023)	2.47 (0.30)	0.59
		ERE-1-3	51.00	5.58	0.64	0.60	6.48	0.0737 (0.030)	2.01 (0.36)	0.58
		ERE-1-4	51.50	5.61	1.34	0.84	6.06	0.331 (0.040)	2.24 (0.34)	0.53
		ERE-1-5	50.40	5.45	2.82	0.95	6.38	1.11 (0.052)	1.95 (0.35)	0.38
P (MPa)	100	ERE-5-A	49.60	3.26	0.04	0.12	4.16	0.0030 (0.019)	1.11 (0.22)	0.19
$^iC^m_{Cl}$ (wt.%)	0.09	ERE-5-1	50.40	3.29	0.11	0.20	4.28	0.0052 (0.020)	1.03 (0.23)	0.19
Duration (h)	66	ERE-5-2	50.20	3.41	0.19	0.28	4.26	0.0074 (0.021)	1.17 (0.22)	0.19
		ERE-5-3	50.60	3.42	0.39	0.47	4.29	0.0145 (0.026)	1.14 (0.23)	0.19
		ERE-5-4	50.70	3.42	0.82	0.89	4.03	0.0310 (0.039)	1.25 (0.22)	0.18
		ERE-5-5	50.70	3.43	1.78	1.14	4.51	0.4305 (0.051)	0.99 (0.24)	0.02
P (MPa)	50	ERE-11-A	49.30	1.88	0.02	0.10	2.78	0.0012 (0.018)	0.47 (0.14)	0.68
$^iC^m_{Cl}$ (wt.%)	0.09	ERE-11-1	49.40	1.93	0.07	0.16	2.31	0.0018 (0.019)	0.77 (0.12)	0.68
Duration (h)	86	ERE-11-2	50.10	1.99	0.11	0.20	2.26	0.0039 (0.019)	0.83 (0.12)	0.67
		ERE-11-3	51.00	1.89	0.22	0.31	2.27	0.0036 (0.022)	0.70 (0.12)	0.67
		ERE-11-4	50.20	1.87	0.45	0.51	2.40	0.0324 (0.026)	0.63 (0.12)	0.65
		ERE-11-5	50.70	1.81	0.95	0.83	2.50	0.140 (0.037)	0.49 (0.13)	0.56
P (MPa)	25	ERE-3-A	50.80	1.38	0.02	0.10	1.48	0.0029 (0.018)	0.62 (0.08)	0.74
$^iC^m_{Cl}$ (wt.%)	0.09	ERE-3-1	49.80	1.55	0.05	0.14	1.72	0.0049 (0.019)	0.67 (0.09)	0.74
Duration (h)	73	ERE-3-2	50.70	1.52	0.08	0.17	1.80	0.0043 (0.019)	0.59 (0.09)	0.74
		ERE-3-3	50.50	1.62	0.18	0.27	1.79	0.0096 (0.021)	0.70 (0.09)	0.74
		ERE-3-4	50.30	1.38	0.33	0.41	1.61	0.0203 (0.024)	0.55 (0.08)	0.73
		ERE-3-5	50.30	1.75	0.91	0.80	1.73	0.140 (0.036)	0.85 (0.09)	0.68
P (MPa)	25	ERE-6-A	49.70	1.38	0.02	0.10	1.57	0.0026 (0.018)	0.59 (0.08)	0.74
$^iC^m_{Cl}$ (wt.%)	0.09	ERE-6-1	49.80	1.65	0.06	0.14	1.70	0.0053 (0.019)	0.78 (0.09)	0.74
Duration (h)	88.5	ERE-6-2	50.90	1.71	0.10	0.17	1.74	0.0088 (0.019)	0.80 (0.09)	0.74
		ERE-6-3	50.60	1.89	0.22	0.28	1.43	0.0224 (0.021)	1.15 (0.07)	0.74
		ERE-6-4	51.20	2.20	0.52	0.53	1.47	0.0609 (0.027)	1.43 (0.08)	0.73
		ERE-6-5	51.20	2.56	1.32	0.93	1.56	0.299 (0.042)	1.73 (0.08)	0.67
P (MPa)	20	ERE-4-A	49.70	1.48	0.02	0.09	1.40	0.0082 (0.018)	0.78 (0.07)	0.73
$^iC^m_{Cl}$ (wt.%)	0.09	ERE-4-1	50.60	1.65	0.06	0.13	1.41	0.0127 (0.019)	0.92 (0.07)	0.73
Duration (h)	72	ERE-4-2	51.60	1.71	0.10	0.17	1.45	0.0132 (0.019)	0.95 (0.08)	0.73
		ERE-4-3	50.10	1.71	0.19	0.27	1.44	0.0169 (0.021)	0.98 (0.07)	0.73
		ERE-4-4	50.60	1.79	0.43	0.47	1.50	0.0430 (0.025)	1.02 (0.08)	0.72
		ERE-4-5	50.40	2.02	1.05	0.86	1.47	0.187 (0.038)	1.25 (0.08)	0.67
P (MPa)	10	ERE-7-A	59.60	1.09	0.01	0.10	0.75	0.0054 (0.019)	0.64 (0.05)	0.74
$^iC^m_{Cl}$ (wt.%)	0.09	ERE-7-1	60.00	1.07	0.04	0.11	0.98	0.0067 (0.019)	0.47 (0.06)	0.74
Duration (h)	108	ERE-7-2	60.90	1.23	0.07	0.14	0.62	0.0110 (0.019)	0.85 (0.04)	0.74
		ERE-7-3	58.90	1.08	0.12	0.18	0.96	0.0166 (0.020)	0.51 (0.06)	0.73
		ERE-7-4	63.70	1.14	0.27	0.27	1.03	0.0388 (0.022)	0.48 (0.07)	0.71
		ERE-7-5	61.20	1.08	0.55	0.48	0.92	0.0723 (0.028)	0.51 (0.06)	0.69

[a] Values in parenthesis are calculated absolute errors.

run at 25 MPa was repeated for different durations (ERE3 for 88.5 h and ERE6 for 73 h) in order to verify the attainment of equilibrium. One Cl-free capsule was run at 50 MPa to check the value of water solubility in a pure H_2O system.

2.3. Characterization of the experimental products

After quench, capsules were weighed, punctured and stored in a drying oven at 120 °C for 20–30 min in order to check for the presence of a quenched fluid phase during the experiments. Chips of glass were then recovered and prepared for analysis. Some were mounted in epoxy for EMPA analyses, and others doubly polished for FTIR spectroscopy.

2.4. Major oxides and Cl analyses

We analysed major elements and Cl in the experimental glasses using a Cameca SX 50 electron microprobe at the BRGM-ISTO joint analytical facility. We used an accelerating voltage of 15 kV, a 10-μm defocused beam to minimize the migration of alkalis and Cl, a beam current of 10 nA, and counting time of 10 s on the peak of all the elements except chlorine, which was counted for 30 s. Backgrounds were counted for half the time of the peak. The calibration was made using analbite for Si and Na, corundum for Al, magnetite for Fe, pyrophanite for Ti and Mn, olivine for Mg, orthoclase for K, andradite for Ca, apatite for P and vanadinite for Cl. In order to verify the homogeneity of the glasses, each time two or three chips of the same experimental charge were analysed for a total of at least ten analyses per chip of glass. A few analyses were made at the same beam conditions in the Au capsules to check for iron loss into the capsule walls with an estimated Fe detection limit of 500 ppm. Sodium loss was addressed by tests with different beam currents on high-pressure, water-rich samples and on low-pressures, water-poor samples. These tests led us to select the above reported beam conditions and assign a relative analytical uncertainty of 5% on Na and K. The Supplementary information shows that alkali loss by EMPA has a negligible influence on mass balance calculations of Cl. For the other elements, the relative uncertainty was between 1 and 7%. CoPdO sensors were analysed using an accelerating voltage of 15 kV and a beam current of 20 nA.

2.5. H_2O analyses

H_2O dissolved in the experimental glasses was measured by FTIR spectroscopy on chips doubly polished at various thicknesses, from 40 to 300 μm (measured by using a micrometre whose accuracy is ±3 μm). We used a Nicolet 760 Magna FTIR spectrometer with an attached optical microscope equipped with a liquid N_2 cooled MCT/A detector (mercury cadmium telluride detector). Resolution was set to 2 cm^{-1} and a white-light source with a CaF_2 beamsplitter was employed in the near-IR region (2000–8000 cm^{-1}). Spectra were obtained on a 100-micron diameter region by accumulating 512 scans. Three to seven spots were analysed on each sample and the results were then averaged.

The structurally-bonded hydroxyl groups (OH^-) and the molecular water (H_2O_{mol}) concentrations were calculated applying the Beer–Lambert law to measured absorbance of the 4500 cm^{-1} and 5200 cm^{-1} bands, respectively. The sum of OH^- and H_2O_{mol} concentrations gives the total water abundance for each spot. Due to the small size of the glass chips, density was not directly measured but determined using the linear regression of Iacono-Marziano et al. [25] for K-phonolitic melt compositions. Molar absorption coefficients from Carroll and Blank [12] were used: $H_2O_{mol} = 1.1$ and $OH^- = 1.25\ L\ cm^{-1}\ mol^{-1}$ with a tangential baseline correction. The accuracy of our FTIR analyses is estimated to be ~10% relative for total H_2O.

2.6. Computing the fluid phase composition and estimating the associated uncertainties

In order to reduce additional sources of error, we ran at each pressure a complete series of capsules with different fluid compositions. The need to fit six or seven capsules in the sample holder to reduce the effects of thermal gradients and to guarantee a good quench of the melt led us to use a limited amount of sample rock powder (about 50 mg) and fluid phase (around 10% relative to powder). The minute amount of fluid left after the experiment prevented its recovery for direct analysis. We thus determined the composition of the fluid phase by mass balance, based on the quantities of glass and solutions weighed before the experiments and the chemical species analysed in the quenched melt (alkalis, Cl and H_2O; [1]. Since the initial and final quantities of Fe, Na, and K in glass were measured by EPMA, it is possible to include these elements in the mass balance. The combined effects of their large abundances in the melt and the small amount of fluid phase, however, induce large error values in the mass balance, making the composition of the fluid phase too uncertain to be useful (see Supplementary information; [69]. The first step of our mass balance thus only includes H_2O and Cl:

$$W^f_{\mathrm{Cl}} = {}^iC^m_{\mathrm{Cl}}\,{}^iW_{\mathrm{gl}} + B\,{}^iW_{\mathrm{alk}} - C^m_{\mathrm{Cl}}W_{\mathrm{gl}} \tag{1}$$

$$W^f_{\mathrm{H2O}} = {}^iW_{\mathrm{H2O}} - C^m_{\mathrm{H2O}}W_{\mathrm{gl}} \tag{2}$$

$$W_{\mathrm{gl}} = {}^iW_{\mathrm{gl}}\frac{1 - A\,{}^iC^m_{\mathrm{Cl}}}{1 - AC^m_{\mathrm{Cl}} - C^m_{\mathrm{H2O}}} \tag{3}$$

$$A = 1 + \frac{M_{\mathrm{Na}}f}{M_{\mathrm{Cl}}(1+f)} + \frac{M_K}{M_{\mathrm{Cl}}(1+f)} \tag{4}$$

$$B = \frac{M_{\mathrm{Cl}}(1+f)}{M_{\mathrm{NaCl}}f + M_{\mathrm{KCl}}} \tag{5}$$

where W is mass, C is mass fraction, M is molar mass, and f is the molar ratio Na/K = 2.4. Subscripts are species except gl and alk that refer to glass and to the added alkalis, (Na–K)Cl, respectively. Superscripts i, m, and f are initial, melt and fluid, respectively. Chlorine in the fluid phase is associated to cations available in the system (H, Na, K, Mn, Ca, Fe, ...). To reduce the number of cases to treat, we consider only the three most abundant, H, Na, and K, as possible Cl-linked cations (e.g., [52]. The second step of the mass balance thus adds various amounts of these three cations as a function of W^f_{Cl}. The three respective end-member masses of cations are calculated by assuming that charge balance with Cl is respected:

$$W^f_j = W^f_{\mathrm{Cl}}\frac{M_j}{M_{\mathrm{Cl}}} \tag{6}$$

where the subscript j corresponds to either H, Na, or K. The three respective equivalent concentrations of HCl, NaCl, and KCl are obtained by:

$${}^{eq}C^f_{jCl} = \frac{W^f_j + W^f_{\mathrm{Cl}}}{W^f_j + W^f_{\mathrm{Cl}} + W^f_{\mathrm{H2O}}} \tag{7}$$

These three assumed cation types yield each a water amount in the fluid phase, ${}^{\mathrm{eq\text{-}HCl}}C^f_{\mathrm{H2O}}$, ${}^{\mathrm{eq\text{-}NaCl}}C^f_{\mathrm{H2O}}$, and ${}^{\mathrm{eq\text{-}KCl}}C^f_{\mathrm{H2O}}$, respectively. Conversion from mass fraction, C, to mole fraction, X, is carried out using:

$$X_j = \frac{C_j/M_j}{\sum_k C_k/M_k} \tag{8}$$

where subscripts j and k indicate the species considered.

An uncertainty is associated with every measured element of the mass balance and the way it propagates through the mass balance calculation determines the final uncertainty of the calculated species proportions in the fluid phase. We performed an algebraic propagation of uncertainties assuming they were independent [60]:

$$\begin{aligned}\Delta\%W^2_{\mathrm{gl}} = {}& \Delta\%{}^iW^2_{\mathrm{gl}} + \left(\frac{{}^iC^m_{\mathrm{Cl}}A}{1 + {}^iC^m_{\mathrm{Cl}}}\right)^2 E_1 \\ & + \left(1 - C^m_{\mathrm{H2O}} - C^m_{\mathrm{Cl}}\right)^{-2}\left[\Delta C^{m\ 2}_{\mathrm{H2O}} + \left(C^m_{\mathrm{Cl}}A\right)^2 E_2\right]\end{aligned} \tag{9}$$

$$E_1 = \Delta\%{}^iC\mathrm{Cl}^{m2} + \Delta\%A^2 \tag{9a}$$

$$E_2 = \Delta\%C\mathrm{Cl}^{m2} + \Delta\%A^2 \tag{9b}$$

$$\Delta A = \frac{\Delta f}{M_{\mathrm{Cl}}(1+f)^2}\sqrt{M^2_{\mathrm{Na}} + M^2_K} \tag{10}$$

$$\Delta\%B^2 = \left(\frac{\Delta f}{1+f}\right)^2 + \left(\frac{\Delta f}{M_{\mathrm{Na}}/M_{\mathrm{K}} + f}\right)^2 \tag{11}$$

$$\begin{aligned}\Delta W\mathrm{Cl}^{f\,2} = {}& \left(\Delta{}^iC^m_{\mathrm{Cl}}{}^iW_{\mathrm{gl}}\right)^2 + \left({}^iC^m_{\mathrm{Cl}}\Delta{}^iW_{\mathrm{gl}}\right)^2 + \left({}^iW_{\mathrm{alk}}\Delta B\right)^2 \\ & + \left(\Delta{}^iW_{\mathrm{alk}}B\right)^2 + \left(\Delta C^m_{\mathrm{Cl}}W_{\mathrm{gl}}\right)^2 + \left(C^m_{\mathrm{Cl}}\Delta W_{\mathrm{gl}}\right)^2\end{aligned} \tag{12}$$

$$\Delta W^{f\ 2}_{\mathrm{H2O}} = {}^iW^2_{\mathrm{H2O}} + \left(\Delta C^m_{\mathrm{H2O}}W_{\mathrm{gl}}\right)^2 + \left(C^m_{\mathrm{H2O}}\Delta W_{\mathrm{gl}}\right)^2 \tag{13}$$

$$\Delta\%{}^{\mathrm{eq}}C^f_j = \sqrt{\Delta\%W^{f\ 2}_{\mathrm{Cl}} + \Delta\%W^{f\ 2}_{\mathrm{H2O}}}\left(1 - {}^{\mathrm{eq}}C^f_j\right) \tag{14}$$

$$\Delta\%{}^{\mathrm{eq}-j}C^f_{\mathrm{H2O}} = \Delta{}^{\mathrm{eq}}C^f_j\left(1 - {}^{\mathrm{eq}}C^f_j\right){}^{\mathrm{eq}}C^f_j \tag{15}$$

where Δx is the absolute uncertainty on the variable x, the symbol $\Delta\%x$ means $\Delta x/x$, and j stands for HCl, NaCl, and KCl, respectively. We associated an uncertainty of 7% on the chlorine in the experimental glasses measured by EMPA, $\Delta\%{}^iC^m_{\mathrm{Cl}}$ and $\Delta\%C^m_{\mathrm{Cl}}$, 10% on the H_2O in the glasses measured by FTIR spectroscopy, $\Delta\%{}^iC^m_{\mathrm{H2O}}$ and $\Delta\%C^m_{\mathrm{H2O}}$. We used a 0.1 precision for the Na/K ratio in the added (Na–K)Cl solution, Δf, and we used the precision of the balance of 0.01 mg for the weighed glass powder, $\Delta{}^iW_{\mathrm{gl}}$, and for the solutions added in the capsules, $\Delta{}^iW_{\mathrm{alk}}$ and $\Delta{}^iW_{\mathrm{H2O}}$. As shown in the Supplementary information, the assumption that the individual uncertainties listed above are independent is only partially correct as some co-vary due to machine (EMPA) consistency [54]. The error propagation (Eqs. (9), (9a), (9b), (10), (11), (12), (13), (14), (15)) thus overestimates the uncertainties on the fluid phase composition, yielding negative lower bounds for W^f_{Cl}. Rather than attempting to quantify these covariations, we used results of the duplicated experimental series at 25 MPa (ERE3 and ERE6) to estimate a realistic maximum relative uncertainty. Of the twelve 25 MPa runs, eight have total relative amounts of Cl and H_2O within 15% of each other (respectively $({}^iC^m_{Cl}\,{}^iW_{gl} + B^iW_{alk})/W_{tot}$ and ${}^iW_{H2O}/W_{tot}$ with $W_{tot} = {}^iW_{gl} + {}^iW_{alk} + {}^iW_{H2O}$). These four pairs of runs (charges #A, #1, #2, and #3) have respective W^f_{Cl} values within 5–50% of each other, so we capped the maximum values of $\Delta\%W^f_j$ and $\Delta\%^{eq}C^f_j$ to 50% (Supplementary information). This adjustment explains the choice of basing $\Delta\%^{eq\text{-}j}C^f_{H2O}$ on $\Delta^{eq}C^f_j$ instead of ΔW^f_{H2O} in Eq. (15).

2.7. The thermodynamical model D-Compress

The fugacity-based model of equilibrium degassing D-Compress [7,8] has been adapted to the context of the Erebus phonolitic system by Burgisser et al. [9]. Here, we extend this model for chlorinated species by using our new solubility data for chlorine. In summary, the augmented model calculates the equilibrium gas composition of 12 species (previously 10): H_2O, H_2, O_2, SO_2, H_2S, S_2, CO_2, CO, CH_4, Cl_2, and HCl. These species are in equilibrium at all times through the following reactions [57]:

$$H_2O = H_2 + \frac{1}{2}O_2 \tag{16}$$

$$H_2S + \frac{1}{2}O_2 = \frac{1}{2}S_2 + H_2O \tag{17}$$

$$SO_2 = \frac{1}{2}S_2 + O_2 \tag{18}$$

$$\frac{1}{2}CO_2 + H_2O = \frac{1}{2}CH_4 + O_2 \tag{19}$$

$$CO + \frac{1}{2}O_2 = CO_2 \tag{20}$$

$$OCS + H_2O = CO_2 + H_2S \tag{21}$$

$$Cl_2 + H_2 = 2HCl \tag{22}$$

The first six equations have been largely described in Burgisser and Scaillet [7] and Burgisser et al. [8], Burgisser et al. [9]. In order to implement reaction (22) into the model, we calculated the equilibrium constant after Symonds and Reed [57] using a temperature-dependent equation of the type:

$$\log(K_{22}) = l_0 + l_1T^{-1} + l_2T + l_3T^{-2} + l_4\log(T) \tag{23}$$

where K_{22} is the equilibrium constant of reaction (22) and l_{0-4} are constants listed in GASTHERM, the values of which are given in Symonds and Reed [57].

The model D-Compress assumes mass conservation of the volatile elements at each pressure step and the gas is composed of the 12 volatile species listed above:

$$\sum_{j=1}^{12} X_j = 1 \tag{24}$$

where X_j is the mole fraction of the species in gas. It also ensures strict conservation of the total (dissolved and gaseous) amounts of elemental volatile species (S, O, H, C and Cl). It considers the gas as an ideal mixture of non-ideal gases, and it takes into account the oxygen-fugacity buffering role of dissolved Fe as a balance of Fe_2O_3 and FeO. Although the model calculates the respective dissolved contents of SO_2 and H_2S, we simply use here the total dissolved S content, $C^m{}_S$, calculated as $(C^m{}_{SO2}/M_{SO2}+C^m{}_{H2S}/M_{H2S}) \times M_S$. Relative errors on $C^m{}_{SO2}$ and $C^m{}_{H2S}$ reported in Burgisser et al. [9] are added to yield the uncertainties on $C^m{}_S$ (+17% and −31% at 100 MPa).

Errors on equilibrium temperature determinations with the previous version of D-Compress, which included reactions ((16)–(21)) and no Cl-bearing species, were assessed in Burgisser et al. [9] thanks to high-temperature fumarole measurements by Taran et al. [58]. We used the same sample, TK1391, to assess how the addition of reaction (22) affects model accuracy. The Cl-bearing version of D-Compress replicates the measured ratios of H_2S/SO_2, CO_2/SO_2, CO_2/CO, CO_2/H_2O, and CO_2/HCl of sample TK1391 at atmospheric pressure for a temperature of 906 °C, which is within <1 °C of that determined by the Cl-free version of D-Compress [9], and which compares well with the 910 °C measured by thermocouple [58]. We thus consider that D-Compress can estimate equilibrium temperatures to an unchanged accuracy of ±5 °C. Other sources of model uncertainties are listed in Burgisser et al. [9] and reported graphically in all the figures of the present work. The model is calibrated to about 300 MPa for all the species except HCl, for which we consider the model calibrated up to 100 MPa (see Results section).

D-Compress operates either by decompressing, or by compressing the magma. In the first case, the input data are the volatile composition of the melt at depth, and the model solves the system for every pressure step decrease, calculating the composition of the gas phase in equilibrium with it (in closed system). In the second case, which we use here to carry out backward tracking of volcanic gases, the input data are the equilibrium compositions of the exsolved species measured in the gas plume emitted from the lava lake, and the model solves the system by recompressing exsolved and dissolved volatiles up to a given pressure.

To calculate the input gas composition, the method of solution used in Burgisser et al. [9] was to fix pressure, temperature, f_{H2O}, f_{H2}, f_{CO2}, FeO*, and the weight fraction of gas. This method proved cumbersome to find equilibrium temperatures as gas measurements were given as species molar ratios (e.g., CO_2/H_2O, CO_2/HCl) and not as fugacities. We thus adapted the method of solution to automate conversion between gas molar ratios and equilibrium temperature. In this new method, pressure, FeO*, and the weight fraction of gas are fixed by the user (for Erebus, 0.065 MPa, 5 wt.%, and 0.45 wt.%, respectively) and the measured molar ratios are used to find the equilibrium temperature. Molar ratios, R_l, of species j and k are converted into fugacity ratios by using

$$R_l = \frac{f_j}{f_k} = \frac{X_j}{X_k}\frac{\gamma_j}{\gamma_k} \tag{25}$$

where $X_{j,k}$ are the respective species mole fractions and $\gamma_{j,k}$ are the respective species fugacity coefficients [8]. Although they are close to unity at atmospheric pressure, most $\gamma_{j,k}$ are calculated using empirical relationships valid up to 300 MPa so as not to lose generality and to be consistent with compression calculations. Exceptions are γ_{Cl2}, which is assumed to equal one and γ_{OCS}, which follows an experimentally calibrated relationship up to 40 MPa but is assumed constant at higher pressure (more details in [9]). The factor γ_{HCl} was calculated following Holloway [24].

The FTIR spectroscopic measurements for the Erebus plume provide estimates of $R_1 = f_{CO2}/f_{H2O}$, $R_2 = f_{CO2}/f_{CO}$, $R_3 = f_{SO2}/f_{OCS}$, $R_4 = f_{CO2}/f_{HCl}$, and $R_5 = f_{CO2}/f_{SO2}$. Naming K_{16}–K_{22} the constants corresponding to reactions ((16)–(22)), respectively, the fugacities of the 12 species contained in these reactions can be obtained from:

$$f_{O2} = (K_{18}R_2)^2 \tag{26a}$$

$$f_{CO2} = \frac{K_{20}K_{16}}{K_{17}R_3}(f_{O2})^{1.5} \tag{26b}$$

$$f_{H2O} = f_{CO2}/R_1 \tag{26c}$$

$$f_{HCl} = f_{CO2}/R_4 \tag{26d}$$

$$f_{H2} = \frac{f_{H2O}}{K_{16}\sqrt{f_{O2}}} \tag{26e}$$

$$f_{CO} = f_{CO2}/R_2 \tag{26f}$$

$$f_{Cl2} = \frac{f_{HCl}^2}{K_{22} f_{H2}} \tag{26g}$$

$$f_{CH4} = K_{19} f_{CO2} (f_{H2O}/f_{O2})^2 \tag{26h}$$

$$f_{SO2} = f_{CO2}/R_5 \tag{26i}$$

$$f_{S2} = \left(\frac{K_{17} f_{SO2}}{f_{O2}}\right)^2 \tag{26j}$$

$$f_{H2S} = \frac{f_{H2O}\sqrt{f_{S2}/f_{O2}}}{K_{16}} \tag{26k}$$

Mole fractions, X_j, are then obtained using the definition of fugacity (Eq. (25)) and entered into the mass balance (Eq. (24)). The only unknown in this mass balance is then the temperature, which is solved for by using a root-finding algorithm (bisection with binary coded decimal number format that has 26 significant digits to keep sufficient precision). Note that for consistency with the method of solution used in recompression runs [9], OCS is excluded from the mass balance and is calculated a posteriori by:

$$f_{OCS} = \frac{f_{CO2} f_{H2S}}{K_6 f_{H2O}} \tag{27}$$

Including OCS into the mass balance computations would have been possible without altering our results because it changes the equilibrium temperature by <0.004%, which is far less than the ±5 °C accuracy of the model.

3. Results

The experimental products selected as successful for the partitioning study were all glasses with a coexisting quenched fluid phase. The composition of the glasses was analysed by EMPA and FTIR spectroscopy, while the composition of the fluid phase was calculated by mass balance. Scanning electron microscope images (Fig. 1a) show that less than 3 vol.% of crystals is present and that no more than 5 vol.% of bubbles nucleated. On the other hand, the highest Cl charges for the 250 and the 200 MPa experiments showed the presence of about 15–20 vol.% of small holes ($\o \leqslant 3$ μm) that we interpret as imprints of salt crystals dissolved during the polishing. Solid salt was also observed on the inner wall of the capsule during opening (Fig. 1b). Whether these salt crystals are from high P–T equilibrium or result from quench processes cannot be determined. Each experimental charge presents very homogenous glass concentrations of chlorine and H_2O. Moreover, the two experiments performed at the same conditions (ERE3 for 72 h and ERE6 for 88.5 h) yielded very similar results, which confirm that experiment duration of 3 days ensures achievement of equilibrium for this melt composition and in the P–T range investigated.

Due to the low redox conditions [35] and to the relatively high content of Fe in the phonolites from Erebus (i.e. FeO ~5 wt.%), some iron might be lost to the melt at run conditions. Defining iron loss as $(C^m_{FeO} W_{gl} - {}^iC^m_{FeO}\,{}^iW_{gl})/{}^iC^m_{FeO}\,{}^iW_{gl}$, we lost up to 10–40% of the original iron in most charges, the most severe losses being at low pressures. Considering that no detectable iron is present in the Au capsule walls, we infer that it has been exsolved into the fluid phase. However, due to the combination of the large amount of Fe in the melts, the value of the associated measurement uncertainties, and the small fluid quantities at run conditions, a meaningful quantification of Fe in the fluid could not be carried out (see Supplementary information), which led us to leave it out of mass balance calculations (Eqs. ((1)–(5))). A similar reasoning applies to the alkalis Na and K; it is possible to show qualitatively that some were present in the fluid phase, but their respective melt contents and the EMPA measurement uncertainty are too high for them to be included in the mass balance (Supplementary information). The combined effects of ignoring Fe, Na, and K in Eqs. ((1)–(6)) on the values of W^f_{Cl} are below $\Delta\%W^f_{Cl}$ for all charges except ERE11-A and ERE11-1, where differences respectively reach 54% and 57%, which is just above the maximum error cap of 50%. We thus conclude that our uncertainty budget is robust.

3.1. Control of oxygen fugacity

The composition of the metal phase in CoPdO sensors allows the measurement of the f_{H2} of the sensor system [59]. Unfortunately, most of the loaded sensors failed and we could directly determine the prevailing f_{H2} only for series ERE2 and ERE1 (Table 2). For series ERE5 and ERE11, we relied on the measurements of the metal sensors of Moussallam et al. [34], which were run at the same P and T conditions as our experiments. The f_{H2} in runs where a sensor was not available (ERE3, ERE6, ERE4, and ERE7) was derived using a calibration curve of $\log(f_{H2})$ vs. P built from available data at 1000 °C. The missing $\log f_{H2}$ were estimated to two decimal places using this polynomial calibration curve.

There are two ways to calculate f_{H2O} at run conditions. The first relies on the H_2O in the fluid phase determined by mass balance, assuming that all Cl was present as NaCl (${}^{eq\text{-}NaCl}X^f_{H2O}$, Table 3), and on the same γ_{H2O} coefficient as in D-Compress [8]. The second method uses the solubility law of the pure water system [9] to calculate f_{H2O} from C^m_{H2O} (Table 2). The resulting f_{H2O} is then combined with the water dissociation constant (K_{16}, [47] to obtain f_{O2}. Fig. 2 compares the f_{H2O} determined by mass balance to the

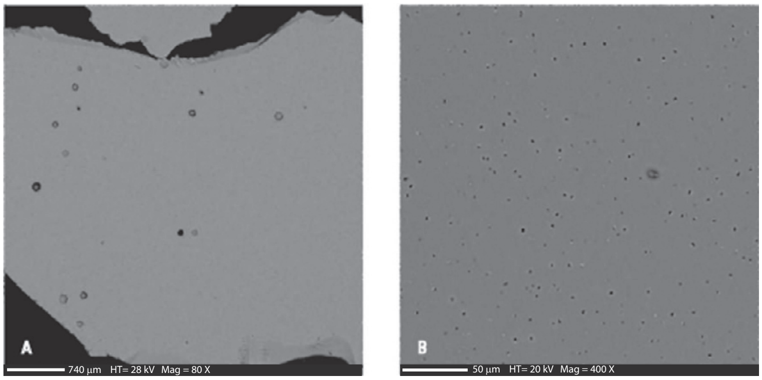

Fig. 1. Backscatter electron images of experimental glasses. (A) A low-Cl charge (ERE3-A) in a 25-MPa experiment with a few (<5 vol.%) micro bubbles. (B) A high-Cl charge (ERE1-5) of the experiment at 200 MPa showing the remnants of salt crystals that apparently dissolved during polishing (black).

Table 3
Composition of the fluid phase at run condition under various assumptions. Symbols are listed in the Methods section. Numbers in parenthesis are relative errors in%.

Sample	${}^{\text{eq-HCl}}C^{f}_{\text{Cl}}$ (wt.%)	${}^{\text{eq-NaCl}}C^{f}_{\text{Cl}}$ (wt.%)	${}^{\text{eq-KCl}}C^{f}_{\text{Cl}}$[a] (wt.%)	${}^{\text{eq}}C^{f}_{\text{NaCl}}$[b] (wt.%)	${}^{\text{eq-NaCl}}X^{f}_{\text{H2O}}$[c] (mol%)	X^{f}_{HCl}[d] (mol%)
ERE-2-A	0.52 (50)	0.52 (50)	0.52	0.85 (50)	99.74 (0.13)	n.s.
ERE-2-1	1.1 (50)	1.1 (50)	1.1	1.9 (50)	99.41 (0.30)	n.s.
ERE-2-2	2.1 (42)	2.1 (42)	2.1	3.4 (42)	98.91 (0.46)	n.s.
ERE-2-3	4.9 (25)	4.7 (25)	4.6	7.8 (25)	97.46 (0.69)	n.s.
ERE-2-4	16 (13)	14 (14)	13	23 (14)	91.39 (1.48)	n.s.
ERE-2-5	38 (11)	30 (12)	27	50 (12)	76.35 (5.55)	n.s.
ERE-1-A	0.22 (50)	0.22 (50)	0.22	0.36 (50)	99.89 (0.06)	n.s.
ERE-1-1	0.64 (50)	0.64 (50)	0.64	1.1 (50)	99.67 (0.16)	n.s.
ERE-1-2	1.0 (50)	1.0 (50)	1.0	1.7 (50)	99.47 (0.27)	n.s.
ERE-1-3	3.5 (43)	3.5 (43)	3.4	5.7 (43)	98.18 (0.82)	n.s.
ERE-1-4	13 (17)	12 (17)	11	20 (17)	93.03 (1.44)	n.s.
ERE-1-5	36 (12)	29 (13)	26	48 (13)	77.63 (5.32)	n.s.
ERE-5-A	0.27 (50)	0.27 (50)	0.27	0.44 (50)	99.86 (0.07)	0.22
ERE-5-1	0.50 (50)	0.50 (50)	0.50	0.82 (50)	99.75 (0.13)	0.41
ERE-5-2	0.63 (50)	0.62 (50)	0.62	1.0 (50)	99.68 (0.16)	0.51
ERE-5-3	1.3 (50)	1.3 (50)	1.2	2.1 (50)	99.36 (0.33)	1.03
ERE-5-4	2.4 (50)	2.4 (50)	2.3	3.9 (50)	98.76 (0.63)	n.s.
ERE-5-5	30 (19)	25 (21)	23	42 (21)	81.89 (5.89)	n.s.
ERE-11-A	0.27 (50)	0.27 (50)	0.26	0.44 (50)	99.87 (0.07)	0.22
ERE-11-1	0.23 (50)	0.23 (50)	0.23	0.38 (50)	99.88 (0.06)	0.19
ERE-11-2	0.47 (50)	0.47 (50)	0.47	0.77 (50)	99.76 (0.12)	0.38
ERE-11-3	0.52 (50)	0.52 (50)	0.52	0.85 (50)	99.74 (0.13)	0.42
ERE-11-4	4.9 (50)	4.8 (50)	4.7	7.8 (50)	97.45 (1.34)	n.s.
ERE-11-5	22 (29)	19 (30)	18	32 (30)	87.28 (5.26)	n.s.
ERE-3-A	0.5 (50)	0.46 (50)	0.46	0.76 (50)	99.76 (0.12)	0.38
ERE-3-1	0.72 (50)	0.72 (50)	0.71	1.2 (50)	99.63 (0.18)	0.59
ERE-3-2	0.73 (50)	0.73 (50)	0.73	1.2 (50)	99.63 (0.19)	0.60
ERE-3-3	1.4 (50)	1.4 (50)	1.3	2.2 (50)	99.30 (0.35)	1.11
ERE-3-4	3.5 (50)	3.5 (50)	3.4	5.7 (50)	98.17 (0.95)	n.s.
ERE-3-5	14 (24)	13 (24)	12	21 (24)	92.32 (2.26)	n.s.
ERE-6-A	0.44 (50)	0.44 (50)	0.44	0.72 (50)	99.78 (0.11)	0.36
ERE-6-1	0.67 (50)	0.67 (50)	0.67	1.1 (50)	99.66 (0.17)	0.55
ERE-6-2	1.1 (50)	1.1 (50)	1.1	1.8 (50)	99.45 (0.28)	0.89
ERE-6-3	1.9 (50)	1.9 (50)	1.9	3.1 (50)	99.02 (0.50)	1.56
ERE-6-4	4.1 (43)	4.0 (43)	3.9	6.6 (43)	97.89 (0.96)	n.s.
ERE-6-5	15 (13)	13 (13)	13	22 (13)	91.93 (1.29)	n.s.
ERE-4-A	1.0 (50)	1.0 (50)	1.0	1.7 (50)	99.47 (0.27)	0.85
ERE-4-1	1.4 (50)	1.3 (50)	1.3	2.2 (50)	99.31 (0.35)	1.11
ERE-4-2	1.4 (50)	1.4 (50)	1.3	2.2 (50)	99.30 (0.35)	1.12
ERE-4-3	1.7 (50)	1.7 (50)	1.7	2.8 (50)	99.13 (0.44)	1.38
ERE-4-4	4.1 (50)	4.0 (50)	3.9	6.5 (50)	97.90 (1.10)	n.s.
ERE-4-5	13 (19)	12 (19)	11	20 (19)	92.97 (1.59)	n.s.
ERE-7-A	0.84 (50)	0.83 (50)	0.83	1.4 (50)	99.57 (0.22)	0.68
ERE-7-1	1.4 (50)	1.4 (50)	1.4	2.3 (50)	99.29 (0.36)	1.13
ERE-7-2	1.3 (50)	1.3 (50)	1.3	2.1 (50)	99.35 (0.33)	1.04
ERE-7-3	3.2 (50)	3.1 (50)	3.1	5.1 (50)	98.37 (0.84)	n.s.
ERE-7-4	7.5 (50)	7.2 (50)	6.9	12 (50)	96.04 (2.15)	n.s.
ERE-7-5	12 (36)	12 (36)	11	19 (36)	93.29 (2.83)	n.s.

[a] Relative errors are the same as for ${}^{\text{eq-NaCl}}C^{f}_{\text{Cl}}$ within meaningful precision.

[b] Values for ${}^{\text{eq}}C^{f}_{\text{H2O}}$ (in wt.%) are given by 100 – ${}^{\text{eq}}C^{f}_{\text{NaCl}}$.

[c] Values for ${}^{\text{eq}}X^{f}_{\text{NaCl}}$ (in mol%) are given by 100 – ${}^{\text{eq-NaCl}}X^{f}_{\text{H2O}}$.

[d] n.s. means not selected for the HCl solubility law because of the possible presence of both vapour and brine and/or significant alkali exchanges between fluid and melt.

water solubility law of Burgisser et al. [9]. The good agreement between the two suggests that both procedures should yield similar results in f_{H2O} and redox state (see Supplementary information for in-depth comparison). We thus simply report in Table 2 the redox state obtained by mass balance. Overall, the oxygen fugacity of our experiments was between QFM and QFM+1 with most charges being between QFM+0.6 and QFM+0.8.

3.2. Melt volatile concentrations

Our experiments were designed to have excess H_2O. This allowed us to measure H_2O solubility in mixed fluid phase experiments (H_2O–Cl). The melt water concentration ranges between 7.35 wt.% at 250 MPa and 0.62 wt.% at 10 MPa (Fig. 2), which compares well with previous studies on pure water solubility at similar experimental conditions [48,9].

Chlorine concentration in the experimental glasses varies between 0.1 and 1.14 wt.% (Table 2). Overall, chlorine concentration in the phonolite increases with pressure from the lowest to the highest initial Cl charge (from charge #A to #5). Fig. 3a shows that Cl in the melt continuously increases in the melt from 10 to 250 MPa for the low-concentration charges #A, #1, and #2, but that for the highest pressure increment, the increase is modest and within uncertainty. The high-concentration charges show a different behaviour (Fig. 3b). Charge #3 reaches a plateau at 200 MPa with 0.6 wt.% of Cl in the melt, while the two highest concentration charges (#4 and #5) reach Cl saturation between 100 and 200 MPa, above which melt Cl content decreases. In charge #4, the Cl dissolved in the melt decreases from 0.89 wt.% at 100 MPa to 0.77 wt.% at 250 MPa. Similarly, the concentration of Cl in the melt in charge #5 reaches a maximum of 1.38 wt.% at 100 MPa and decreases to 0.89 wt.% at 250 MPa. These observations suggest that, at the highest pressure, experiments are near chloride salt saturation even for the charges with low initial Cl content.

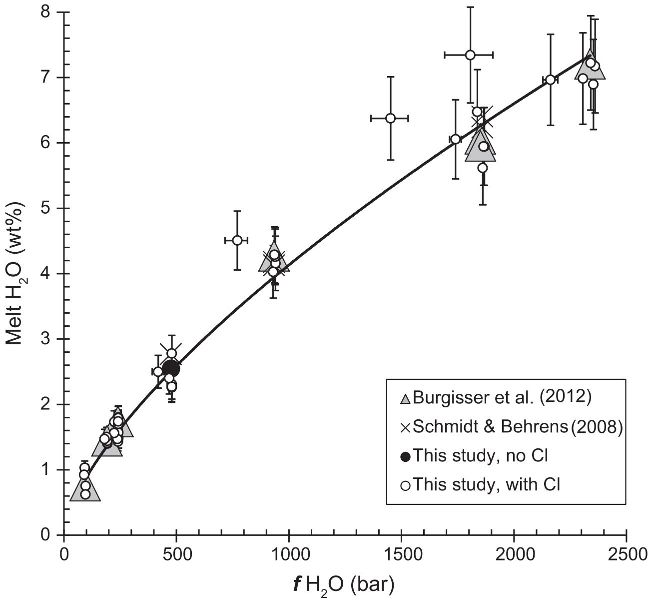

Fig. 2. H_2O solubility in H_2O–Cl experiments compared to pure H_2O experiments. Open circles correspond to the H_2O solubility measured in the chlorine partition experiments of this study; the closed circle is the zero-Cl charge run at 50 MPa to check water solubility in H_2O-pure system. Water fugacities are calculated from the H_2O mole fraction in the fluid phase (see text). We note some variability in certain runs with similar f_{H2O} but an overall good agreement with the H_2O solubilities in other hydrous, Na-phonolitic melts.

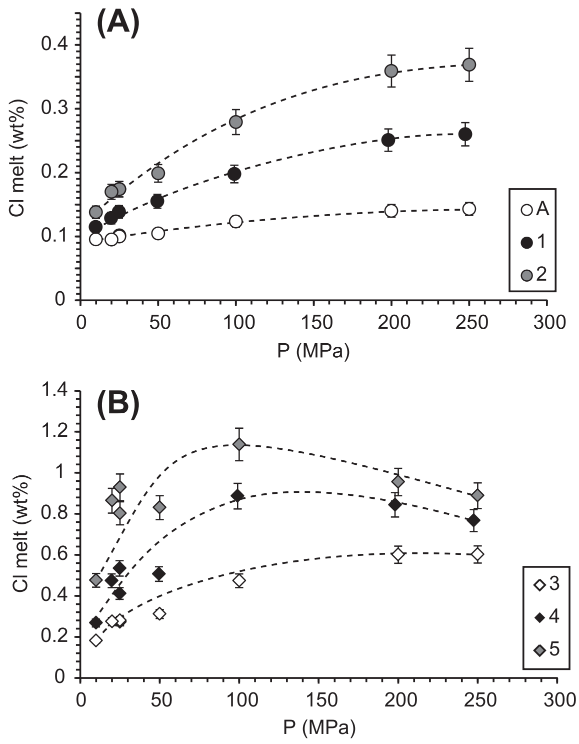

Fig. 3. Overview of the variation of Cl dissolved in the melt (analysed by EMPA) with pressure. Symbols correspond to the different initial charges of Cl introduced as hydrous saline solutions (#A≃0.2 mol/kg, #1≃0.5 mol/kg, #2≃0.8 mol/kg, #3≃1.6 mol/kg, #4≃3.0 mol/kg, and #5≃5.3 mol/kg). See text for the interpretation of the hand-drawn trends. (A) Low-Cl charges, (B) high-Cl charges.

3.3. Composition of the fluid phase

The composition of the fluid phase was calculated by first neglecting cations such as H, Na, K, or Fe (Eqs. ((1)–(5))), and then assuming that each Cl anion was linked to one of H, Na, or K (Eqs. (6), (7), Table 3). This assumption leads to three possible Cl fluid concentrations, ${}^{\text{eq-HCl}}C^f_{\text{Cl}}$, ${}^{\text{eq-NaCl}}C^f_{\text{Cl}}$, and ${}^{\text{eq-KCl}}C^f_{\text{Cl}}$. The difference between ${}^{\text{eq-NaCl}}C^f_{\text{Cl}}$ and ${}^{\text{eq-KCl}}C^f_{\text{Cl}}$ is <12%, which is systematically lower than the uncertainty on Cl mass balance ($\Delta^{\text{eq}}C^f_{\text{Cl}}$, Eq. (14) and Table 3), so only ${}^{\text{eq-HCl}}C^f_{\text{Cl}}$ and ${}^{\text{eq-NaCl}}C^f_{\text{Cl}}$ were given further consideration for simplicity. Fig. 4 displays the Cl fluid content as a function of pressure. The Cl fluid content varies widely from 0.22 to 38 wt.% across the experimental suite. The difference between ${}^{\text{eq-HCl}}C^f_{\text{Cl}}$ and ${}^{\text{eq-NaCl}}C^f_{\text{Cl}}$ is larger than symbol sizes at the scale of Fig. 4 only for charges #4 and #5, so only ${}^{\text{eq-HCl}}C^f_{\text{Cl}}$ is displayed for all other charges for clarity. Assuming a particular cation type associated with Cl thus affects Cl fluid concentrations less than mass balance precision, except for the two samples that have the highest C^f_{Cl} and pressures (ERE1-5 and ERE2-5). In the most Cl-rich charge at any given pressure (#5), Cl in the fluid phase increases from 12 wt.% at 10 MPa to 38 wt.% at 250 MPa. In the other charges (#A-#4), notwithstanding the large uncertainties in the mass balance calculations (up to 50% on C^f_{Cl}), Cl systematically reaches a minimum concentration between 50 and 100 MPa.

Fig. 5 shows the concentration of chlorine in the fluid phase, ${}^{\text{eq-HCl}}C^f_{\text{Cl}}$, as a function of the concentration of chlorine in the melt, C^m_{Cl}. The highly non-ideal behaviour of the chloride–H_2O system under the investigated conditions is obvious on these plots and has been underlined by hand-drawn dashed lines. Such non-ideal behaviour has been documented for several melt compositions [54,55,51,49,50,65,67,68,69,56,1] and is enhanced in the region where the fluid encounters a miscibility gap. We observe some salt deposits only in the highest Cl-charged capsules at 250 and 200 MPa, but the results shown in Figs. 3 and 4 suggest that the process of hydro-saline formation may occur at significantly lower pressures. Charges #4 and #5, for instance, likely involve brine formation at pressures >100 MPa because C^m_{Cl} decreases at high pressure can readily be explained by Cl capture by the saline phase (Fig. 3).

Before addressing the complexities of fluid immiscibility, the simpler approach of partition coefficient allows us to highlight important, first-order features of the chloride–H_2O–silicate melt system. We can estimate the partition coefficient $D_{\text{Cl}}^{f/m} = C^m_{\text{Cl}}/C^f_{\text{Cl}}$ at each pressure from the slope of a linear interpolation of the data. Fig. 5 shows that the linear fit is possible only at the lowest chloride concentrations (solid lines). Acknowledging this limitation, we calculated $D_{\text{Cl}}^{f/m}$ by restricting the linear fitting to the lowest chloride charges of each experiment at each pressure. Since uncertainties on C^f_{Cl} are large, we used a linear least-squares fit technique that takes uncertainties on both concentrations into account [46]. We included data points into the linear regression until R^2 was maximised, excluding those points at higher concentrations (Fig. 5). Fig. 6 shows $D_{\text{Cl}}^{f/m}$ as a function of pressure. We found that $D_{\text{Cl}}^{f/m}$ ranges between 1.8 and 10, but shows two trends: from 250 to 50 MPa, $D_{\text{Cl}}^{f/m}$ decreases from 5 to 1.8, while from 50 to 10 MPa it increases to reach 10. This behaviour has never been demonstrated previously, owing to the lack of low-*P* experiments.

The immiscibility gap that affects some of our runs can be best understood by using the H_2O–NaCl system and ${}^{\text{eq}}C^f_{\text{NaCl}}$ and ${}^{\text{eqNaCl}}C^f_{\text{H2O}}$ to characterize the fluid phase composition. As is shown below, uncertainties in the phase diagram H_2O–NaCl are large at the *P*–*T* considered [64], which dissuaded us from using a more complete system such as H_2O–NaCl–KCl to understand species relationships in the fluid phase of our experiments. Assuming hereafter that all Cl anions are associated to Na cations, Fig. 7 shows the NaCl fluid composition of our data plotted as a function of pressure (${}^{\text{eq}}C^f_{\text{NaCl}}$, Table 3). Three isotherms delimiting the mixed-fluid phase region from that where a vapour coexists with a high-density liquid we will refer to as brine. The 1000 °C isotherm, which corresponds to our

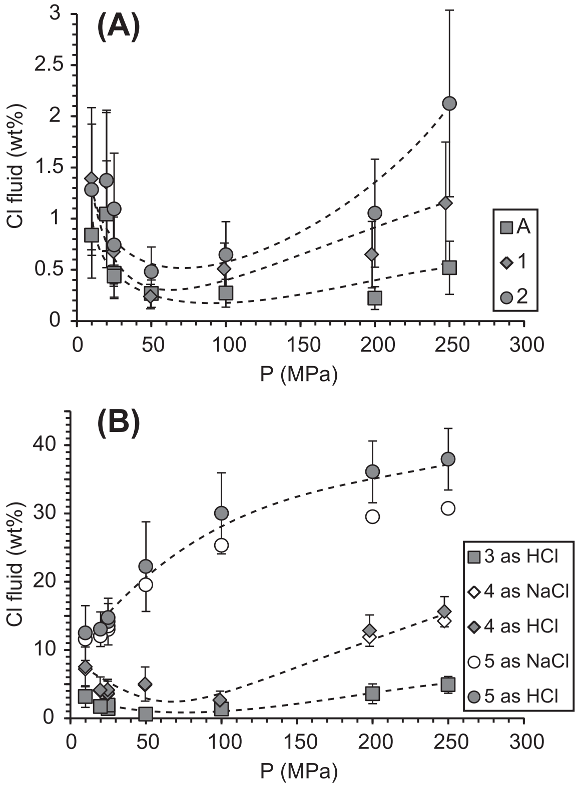

Fig. 4. Cl concentration in the bulk integrated vapour plus brine fluid phase (recalculated by mass balance) as a function of pressure. Symbol shapes correspond to the same charges as in Fig. 3. The charge #5 shows a peculiar trend of Cl in the fluid continuously increasing with pressure. This behaviour is ascribed to the presence of a saline phase capturing chlorine at these very high chloride concentrations, even at the lowest pressures. See text for the interpretation of the hand-drawn trends. (A) Low-Cl charges with chlorine concentrations reported as $^{eq\text{-}HCl}C^{f}_{Cl}$ only. (B) High-Cl charges with chlorine concentrations reported as $^{eq\text{-}HCl}C^{f}_{Cl}$ or $^{eq\text{-}NaCl}C^{f}_{Cl}$.

experimental temperature conditions, was calculated using the model of Driesner and Heinrich [17]. The 800 and 900 °C isotherms are given by the thermodynamical calculations of Anderko and Pitzer [3] and the horizontal arrow indicates how the vapour side of the phase boundary is expected to shift at higher temperature. The horizontal grey shaded bar covers the experimental values obtained by Bodnar et al. [4] at 1000 °C and 100 MPa, which are the only experimental data available to constrain the vapour side of the phase boundary in both models [3,17]. Several arguments suggest that the immiscibility boundary is closer to the low end of the experimental values [4,3]. Notwithstanding this additional constraint, Fig. 7 shows that the vapour end of the immiscibility boundary is poorly constrained at low (<50 MPa) pressures [43], with more than an order of magnitude between the two modelled values of $^{eq}C^{f}_{NaCl}$ at 25 MPa. While some of our data clearly fall in the vapour plus brine field, additional evidence is needed before further data interpretation.

Fig. 8 shows the fluid NaCl-equivalent content as a function of the melt Cl content. In such a plot, increasing the total Cl content in the system at a given pressure and temperature should cause C^{m}_{Cl} to increase monotonically as long as the fluid phase is in the vapour field [30,50]. If increasing the total Cl causes the fluid to unmix, the melt Cl concentration should remain constant as long as the fluid phase remains in the vapour plus brine region. In this case, further total Cl increase would eventually cross the brine side of the immiscibility boundary and cause C^{m}_{Cl} to increase again. If the data points are sparse in the vapour plus brine region, the resulting trend from low to high $^{eq}C^{f}_{NaCl}$ would appear to have an inflexion point when the immiscibility field is crossed. Such behaviour has been documented in magmas by Botcharnikov et al. [6], Signorelli and Carroll [54] and Webster et al. [67] among others.

Fig. 8a shows monotonic C^{m}_{Cl} increases without inflexion points at 200 and 250 MPa, as suggested by manually drawn dashed curves. At 100 MPa, however, it is likely that a plateau in C^{m}_{Cl} is reached around 5 wt.% NaCl equivalent. Fig. 8b shows monotonic C^{m}_{Cl} increases with pressure with one inflexion point at all pressures <100 MPa, as suggested by manually drawn dashed curves. Even considering the large uncertainties in both variables, there are no clear plateaus in C^{m}_{Cl} below 100 MPa. Unlike the peralkaline phonolites studies by Signorelli and Carroll [54], there is no straightforward correspondence between the information given by Figs. 7 and 8. Note that Signorelli and Carroll [54] used molality instead of mass concentration in their analysis, but that recasting our data in molality does not change the trends shown by Fig. 8.

Both models of the NaCl–H_2O system in Fig. 7 agree that the brine side of the immiscibility boundary occurs at salinities >50 wt.% below 100 MPa, way above those of our experiments, so that it is doubtful that the inflexion points in Fig. 8b are due to the crossing of the immiscibility field as salinity increases [30,50]. There may be several reasons for this complex behaviour. First, the H_2O–NaCl system of Fig. 7 is a simplification that does not take into account other cations such as K or Fe likely present in the fluid phase at run conditions. Sodium, as well as K and Fe, are abundant in the melt and these elements partition between melt and fluid at run conditions [22,69]. This and the dissociation of NaCl and H_2O into NaOH and HCl (e.g., [61,29]) likely affect the amount of Cl that can dissolve into the melt. The precision of the phase diagram of the H_2O–NaCl(–KCl) system at high temperature and that of our determinations of the fluid phase composition, however, are not sufficient to further explore these possibilities. Instead, we chose to classify our data into four groups. The first group contains data >100 MPa (diamonds in Fig. 7) that indicate a decrease in C^{m}_{Cl} with increasing total pressure at a given $^{eq}C^{f}_{NaCl}$ (Fig. 8a). The second group comprises the only data point that is in the vapour plus brine field because of likely C^{m}_{Cl} plateau and the agreement in the phase diagrams (black-filled symbol in Figs. 7 and 8). The third group includes data that are in the vapour field because of the monotonic, steep C^{m}_{Cl} increase with increasing pressure and the agreement between the two phase diagrams (white-filled symbols in Figs. 7 and 8). The last group contains all the other data, the status of which (sub- or supercritical) is uncertain (grey-filled symbols in Figs. 7 and 8).

3.4. Backward tracking and decompression simulations from D-Compress

D-Compress can operate either by decompressing the volatile species in equilibrium with the magma, or by compressing them from atmospheric pressure to depth (backward tracking). Here, we adopt the second approach but the observations in the section below are valid for both scenarios.

3.4.1. Choice of solubility data and pressure constraints

The dependence of chlorine speciation upon pressure raises general questions on how to deal with "chlorine" solubility in our fluid/melt system, and, in particular, how to relate it to the fugacity of the chloride species for D-Compress. There is indeed no single "chlorine" solubility, as there are multiple chloride species (e.g., HCl, NaCl, and KCl) in the fluid with occasional coexistence of vapour and brine. However, we can select a subset of experiments that is amenable to modelling the more restricted conditions prevailing in the Erebus magmatic system.

Two constraints are helpful to characterise chlorine behaviour at Erebus. The first is given by Cl content in melt inclusions

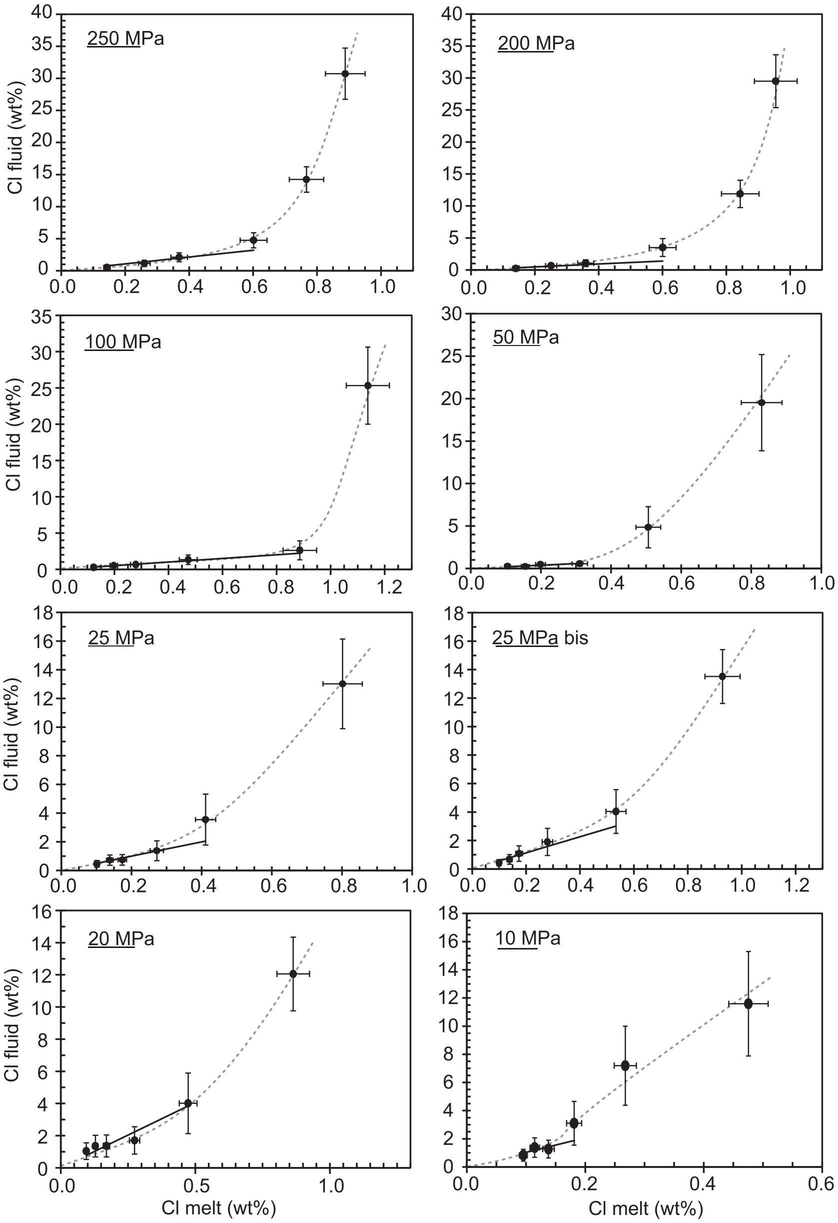

Fig. 5. Cl concentration in the fluid, ${}^{\text{eq-HCl}}C^{f}_{\text{Cl}}$, versus Cl concentration in the melt, C^{m}_{Cl}, at different experimental pressures. Graphs show two regression curves: a linear fit at low Cl content and a hand-drawn curve highlighting the generally non-linear behaviour of each series. The averaged distribution coefficients ($D_{\text{Cl}}^{f/m}$) are derived from the linear fits on the lowest chloride charges (see text).

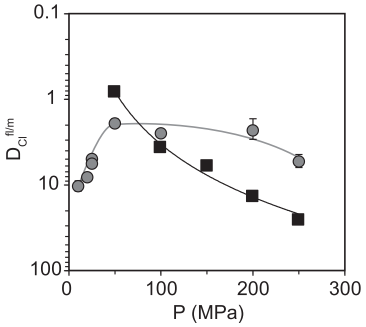

Fig. 6. Variation of $D_{\text{Cl}}^{f/m}$ with pressure for this study (grey circles) and for Signorelli and Carroll [54] (black squares). A clear trend change of our data occurs at the lowest pressures, where Cl strongly partitions in the fluid phase.

(0.13–0.16 wt.%, [41] and in the glass of the bomb we used as starting material (0.09 wt.%, [9]. These values likely frame melt Cl content from depth to the surface, respectively. Figs. 7 and 8 suggest that these small amounts are such that the fluid in equilibrium with Erebus phonolitic melt should be in the vapour field over the pressure range covered by our experiments (10 to 250 MPa). The second constraint is given by FTIR gas chemistry measurements. If a large part of Cl is present in the fluid phase as brine (>5 wt.% NaCl equivalent at 0.1 MPa according to a conservative estimate calculated following Driesner and Heinrich [17], the HCl measured in the gas plume should be far away from its equilibrium value because of the physical separation of brine and vapour above the lava lake surface. Taking as a reference the measured gas composition on 15 December 2010 at 10h40:42 UTC (representative composition, see below), the equilibrium temperature using the Cl-free version of D-Compress [9] is 1022.4 °C. Including Cl in the

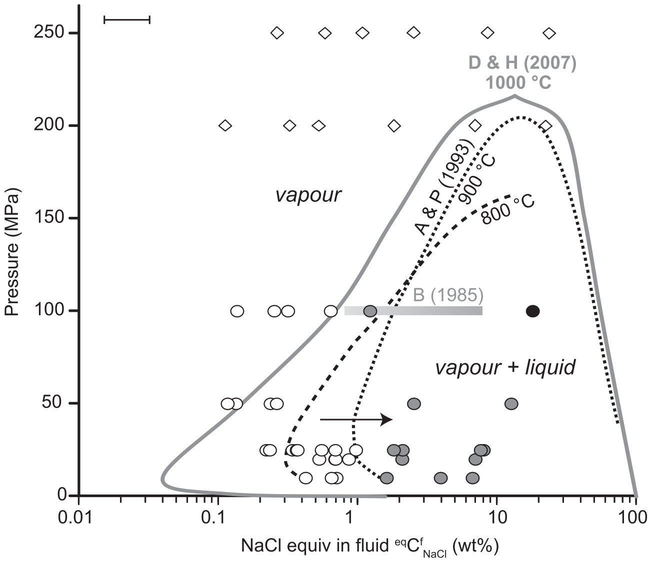

Fig. 7. Phase diagram for the H_2O–NaCl system delimiting the vapour and vapour + liquid fields. Vapour-liquid equilibrium curves in solid grey lines were calculated using the model of Driesner and Heinrich [17] at 1000 °C. Equilibrium curves in dotted (900 °C) and dashed (800 °C) black lines are from the model of Anderko and Pitzer [3], and the horizontal arrow shows the direction in which the 1000 °C curve would be shifted compared to the lower-temperature curves. The horizontal shaded grey bar represents data from Bodnar et al. [4] by which both models are constrained. Symbols mark the fluid phase composition of the runs at different pressures (Table 3), which is reported in NaCl-equivalent content (i.e. considering that each chloride ion in the fluid phase is associated with a sodium ion). The error bar in the upper corner indicates typical data uncertainty. Symbol shapes and colours classify the data into four groups (see text).

calculation (reaction (22)) shifts this temperature to 1022.1 °C, which is a change well below model accuracy. Differences in the SO_2/HCl molar ratio between the measured value and the two calculated values are <0.6%, which means that the content of HCl in the gas is at its equilibrium value. These two lines of evidence thus suggest that Cl at Erebus is unaffected by immiscibility.

Of the four subsets of experiments defined in Fig. 7, the one at low pressures and low salinity (white-filled circles, Table 3) is the least influenced by both immiscibility at high (>~1 wt.% NaCl equivalent) salinities and alkali partition between fluid and melt at high pressure (>100 MPa). Using the observation that in the vicinity of the vapour branch of the immiscibility field, the dissociation of NaCl and H_2O into NaOH and HCl causes the low-density vapour to be enriched in HCl [53,29], we assume that all chlorine in the fluid in those runs was present as HCl, thus neglecting other Cl-bearing species. In other words, we assume that $C^{f}_{HCl} = {}^{eq}C^{f}_{NaCl}$ and we use C^{f}_{HCl} to obtain molar fractions of HCl in the fluid, X^{f}_{HCl}, for this experimental subset (Table 3). Note that assuming instead $C^{f}_{HCl} = {}^{eq\text{-}HCl}C^{f}_{HCl}$ would systematically decrease X^{f}_{HCl} by 37%, within the 50% error. The corresponding f_{HCl} were obtained using total pressure and the γ_{HCl} calculated following Holloway [24]. Fig. 9 shows the concentrations of Cl analysed in the melt versus the f_{HCl} calculated for the coexisting fluid phase. Given the data scatter, we defined three regression curves that would ensure consistent extrapolation of the C^{m}_{Cl}–f_{HCl} relationship to lower fugacities while encompassing the spread of the data. The first curve is a power law representative of all the data contained in the subset:

$$C^{m}_{Cl} = 1.520 \times 10^{-3} f_{HCl}^{0.2264} \qquad (28)$$

The two other curves are maximum and minimum solubility laws based on two extreme fittings (Fig. 9). The maximum law (pre-exponential factor of 2.620×10^{-3} and exponent of 0.1499) is based on six runs that are the furthest from (i.e. that have the largest Euclidian distance above) the globally fitted curve, and the minimum law (pre-exponential factor of 1.005×10^{-3} and exponent of 0.1916) is based on the six runs that are the furthest below the globally fitted curve. The choice of the number of these extreme runs was guided by the constraint that the two extreme laws should frame the whole dataset while not crossing the globally-fitted curve within the value range used to model the Erebus system in the parameter range of interest (grey area in Fig. 9 with the f_{HCl} range obtained a posteriori from model runs). Overall, there is a factor ~5 difference between the maximum and minimum C^{m}_{Cl} predicted by the solubility laws. This uncertainty propagates into D-Compress runs involving gas and melt in a non-linear fashion. Typical closed-system recompression runs with the average law (28) and with the two extremes give, at 100 MPa, +148% and −18% uncertainties on C^{m}_{Cl}, +14% and −19% on X^{f}_{Cl}, and ±16% on the gas molar ratio SO_2/HCl. To simplify interpretation, all model outputs are reported on logarithmic axes and a single error bar is displayed for each graph. This bar is the sum of positive and negative errors at the highest simulated pressure (i.e. errors on simulated C^{m}_{Cl} are ±83%, regardless of pressure).

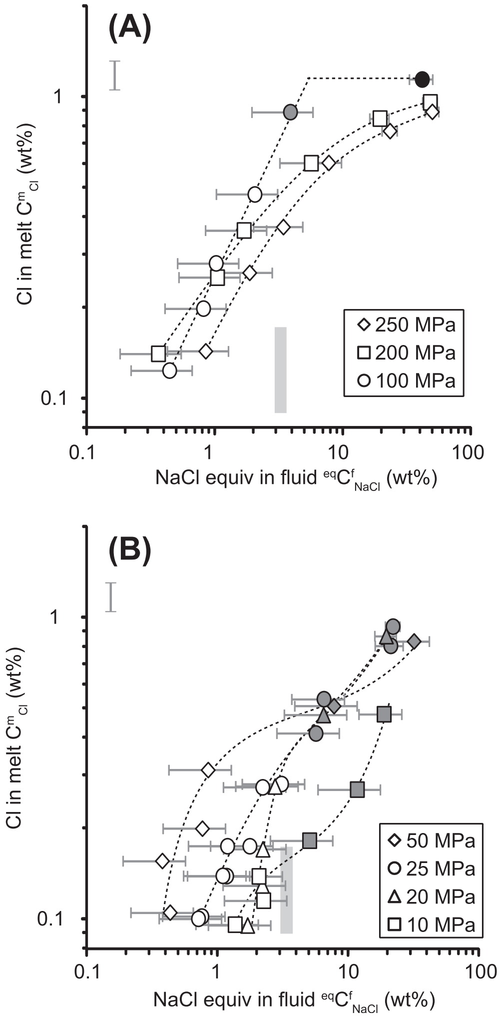

Fig. 8. NaCl equivalent concentration, ${}^{eq}C^{f}_{NaCl}$, in the fluid versus Cl concentration in the melt, C^{m}_{Cl}, at different experimental pressures. Error bars in the upper corner indicates typical data uncertainty on C^{m}_{Cl} and uncertainties on ${}^{eq}C^{f}_{NaCl}$ are shown for each data point. Hand-drawn curves highlight the inferred behaviour of each series. Symbol shapes refer to run pressures. Symbol fillings (white, grey, and black) refer to data classification (see text). (A) High-pressure charges. (B) Low-pressure charges. The light grey area covers the likely conditions at Erebus.

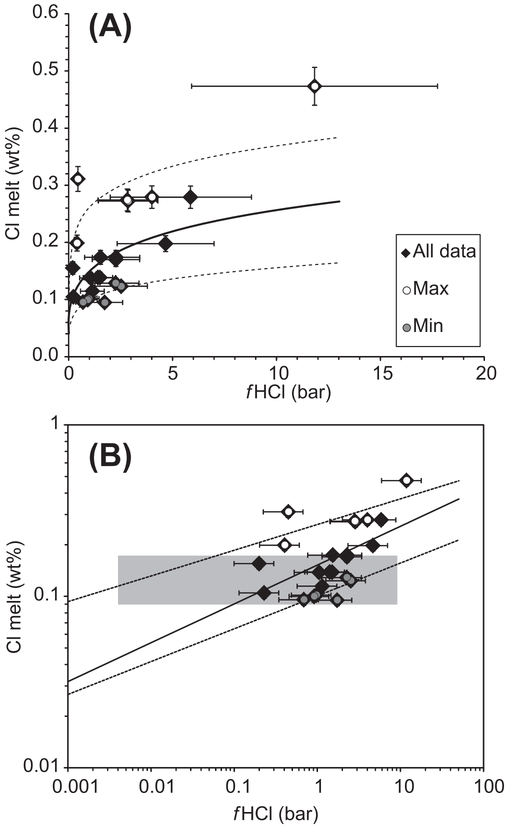

Fig. 9. Cl concentration in the melt, C^{m}_{Cl}, versus HCl fugacity, f_{HCl}. Large diamonds indicate runs assumed to contain mainly HCl and H_2O (Table 3), white (grey) marks flag data selected for maximum (minimum) solubility laws (dashed curves), and solid curves represent the globally-fitted solubility law (Eq. (28)). (A) Linear f_{HCl} scale. (B) Logarithmic f_{HCl} scale. The grey region indicates the f_{HCl} range calculated by the recompression runs modelling Erebus degassing and the C^{m}_{Cl} range measured in matrix glass and glass inclusion in Erebus phonolite.

3.4.2. Backtracking simulations

We analysed 7.5 h of continuous gas measurements made at Erebus by FTIR spectroscopy on 15 December 2010. The gas composition time series consists of five molar ratios of six measured species (CO_2/H_2O, CO_2/CO, CO_2/SO_2, SO_2/OCS, and CO_2/HCl). These were derived from retrievals of absorption spectra collected every ~4.5 s and corrected for atmospheric H_2O and CO_2 (for details on the procedure, see [37,41,9]. These species ratios were used in conjunction with an assumed local atmospheric pressure of 0.065 MPa as input for the thermodynamical model, which was then used to compute the equilibrium temperature and the molar quantities of the six remaining species (Cl_2, O_2, H_2, H_2S, S_2, and CH_4). This procedure yielded the equilibrium temperature of the gases emitted by the lava lake (Fig. 10). The resulting time series contains >6000 equilibrium temperatures, which represents a wealth of information compared to the few gas measurements analysed in previous studies [41,9].

The computed temperatures fluctuate between 743 and 1145 °C (Fig. 10). The average temperature is 1026 °C with a standard deviation of 26 °C, which brings the low temperature range to ~1000 °C and the high temperature range to ~1050 °C. Although few temperatures are hotter than 1050 °C, many data points are well below 1000 °C. Burgisser et al. [9] linked such low temperature peaks to the adiabatic cooling of large gas bubbles exploding at the lake surface. To minimise the effects of such explosions and gain insights into the quiescent behaviour of the lake, we treated the time series in two different ways. Considering that low-temperature peaks are of short duration (on the order of a few samples), a first-order treatment was to apply a running average of 60 samples (4.5 min) to enable visual inspection of the time series for oscillatory behaviour (Fig. 10). While some oscillations can be seen between 04:00 and 05:00 h, the swarm of low temperatures between 4:33 and 4:48 masks the signal. We thus removed all temperature peaks <1000 °C and performed wavelet analyses by splitting the time series into two subsets either side of the hour-long data gap starting at 05:00 h (Fig. 10 b and c). A period of 7–9 min is clearly visible in the first subset (Fig. 10b) whereas the second subset (Fig. 10c) shows higher frequencies superimposed on a signal with ~20-min-period.

To investigate whether low temperature peaks are linked to explosive degassing, we used a concurrent series of digital photographs of the lava lake taken every ~2–3 s during the first part of the day (between 03:47 and 05:00 h). Five small bubble bursts were captured by the digital camera (Fig. 11). In three cases (labels 1–3 in Fig. 11), explosions do not correspond to any apparent temperature variations. However, these events and their associated expelled gases were located outside the line-of-sight of the FTIR spectrometer, which was positioned to view the approximate centre of the lake. Additionally, many troughs apparent in the temperature time series do not correspond to bubble explosions based on the photographic record. However, explosions last for only a second or so and some may not have been recorded due to the photographic acquisition time step of 2–3 s. Also, areas of the lake surface are often obscured by the gas and aerosol plume circulating within crater. However, in two cases (labels 4–5 in Fig. 11), explosions occurred closer to the line-of-sight of the FTIR spectrometer and also correspond to temperature troughs in the time series (743 and 845 °C, respectively). These occurrences suggest that low-equilibrium temperatures correspond to small (metre-sized) bubble bursts.

Recompression of the equilibrium gas compositions, assuming that the gases ascended within a phonolitic melt, has been used to locate a possible common source for the explosive and quiescent gases [9]. The two explosions recorded, however, correspond to ephemeral (one to two samples) low-temperature spikes because of their small sizes. It is thus not possible to estimate measurement precision on such explosions, which hinders the quantitative interpretation of recompressing the gases involved. Large explosions, however, produce geochemical signals that last for long enough to be recorded repeatedly, which gives a measure of uncertainty [41]. We selected one explosion at 09:09 h that is recorded in the gas composition time series for about 10 samples, which corresponds to ~45 s. Five of these samples have similar gas ratios, which correspond to an equilibrium temperature of 838 ± 2.5 °C. This is of the same order as model precision (±5 °C). Although this explosion occurred outside of the observation window of the photographic camera (Fig. 10), its computed equilibrium temperature is close to that of the visually recorded explosion labelled 5 in Fig. 11. As explained in Burgisser et al. [9], the low explosive temperatures stem from adiabatic decompression during bubble burst. Removing the compositional effect of this cooling is carried out by first reheating and recompressing the explosion gas isentropically to the average quiescent temperature, which is assumed to represent lake temperature. The recompression is then carried out to higher pressure isothermally. To represent the quiescent degassing behaviour, we used three geochemical records with computed equilibrium temperatures close to (a) low, (b) average, and (c) high values prevailing during a quiescent period: 1051 °C at 10:37:11, 1022 °C at 10:40:42, and 1003 °C at 10:42:34. We found this method preferable to the selection of representative ratio values used in Burgisser et al. [9] because it is based on representative temperatures instead of representative species ratios.

Following Burgisser et al. [9], we use four simple scenarios to recompress and thus backtrack gas and melt volatile compositions

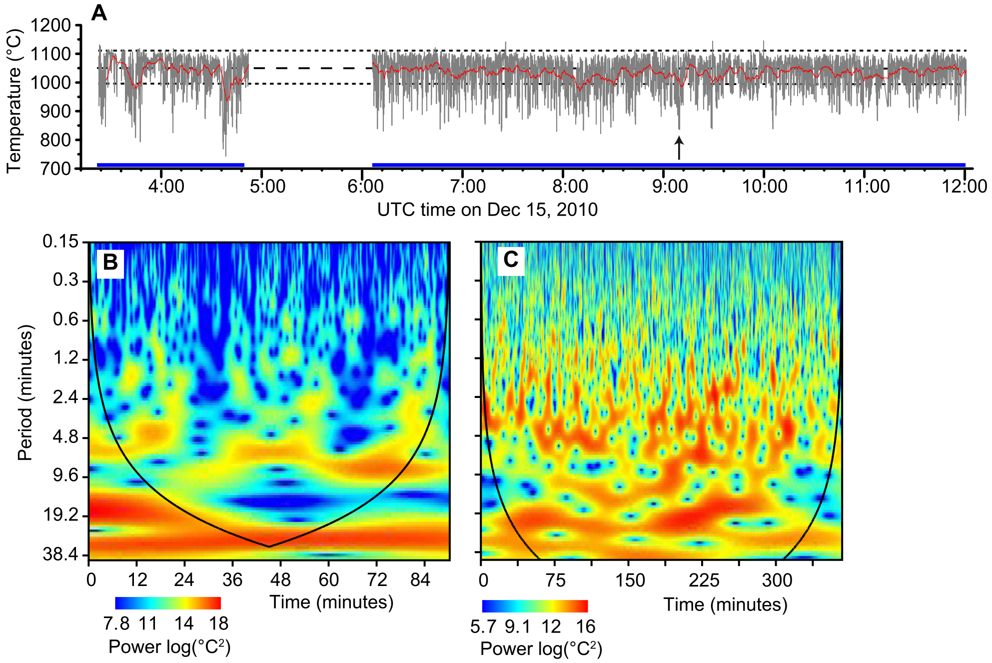

Fig. 10. Temperatures of the gas emitted at the surface of Erebus lava lake on December 15, 2010. (A) Equilibrium temperature of the gas calculated using five ratios of chemical species. The grey curve is the temperature evolution given by one measurement every ~4.5 s, the red curve is a moving average of the grey curve over a window of 4.5 min, the black horizontal dashed line is the average temperature for that day, and the two dotted black horizontal lines represent one standard deviation. The arrow marks the explosion used in backtracking modelling. The two blue lines delimit two subsets of nearly continuous data acquisition over which the frequency analyses in (B and C) were performed. (B) Period content of the first subset (3:22–4:51) by wavelet decomposition. (C) Period content of the second subset (6:06 to 12:00) by wavelet decomposition. For both subsets, Morlet wavelets have been used, hot colours indicate high period intensity, cold colours indicate low period intensity, and black curves indicate the cone of influence of the dataset extremities, below which the period intensities are less reliable. (For interpretation of the references to colour in this figure legend, the reader is referred to the web version of this article.)

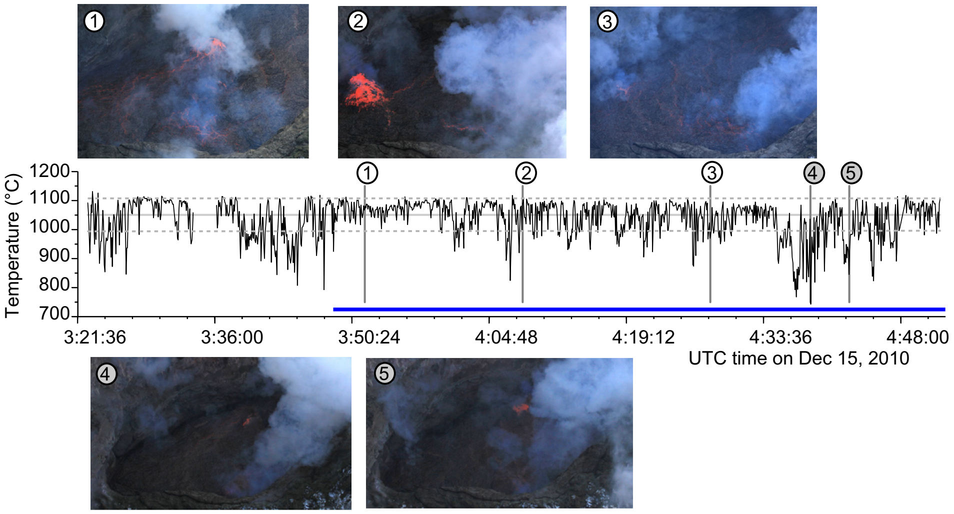

Fig. 11. Evolution of the temperature of the gas emitted at the surface of Erebus lava lake on December 15, 2010 between 3:22 and 4:51 UTC. The black curve is the equilibrium temperature of the gas calculated using five ratios of chemical species every ~4.5 s, which correspond to the first subset of Fig. 10. The grey horizontal line is the average temperature over the whole day and the two dotted grey horizontal lines represent one standard deviation. Numbered black vertical lines marks the times at which explosions were recorded by a digital camera taking pictures every ~2–3 s. The blue horizontal line covers the period over which the picture series was taken. Pictures are numbered according to the vertical lines on the time series and illustrate five recorded explosions. In two occurrences (greyed labels 4 and 5), explosions correspond to a low-temperature signal. (For interpretation of the references to colour in this figure legend, the reader is referred to the web version of this article.)

within the Erebus plumbing system. During passive degassing, the role of the melt surrounding the gas is taken into account by two end-member scenarios. One scenario assumes bi-directional flow where gas and melt rise together as a closed system to reach an arbitrarily fixed porosity at the surface (‘gas+melt’ run). This end-member approaches the behaviour of a slowly convecting magma column. The other end-member assumes that the gas rises independently from any point within the otherwise stationary magma column (‘gas-only’ run). This case represents a stagnant melt column undergoing steady degassing. Explosions, on the other hand, are triggered by large (meter-sized on 15 December 2010) gas bubbles rupturing the lake surface. The behaviour of these large bubbles, conventionally referred to as gas slugs, is also framed by two scenarios. The first end-member assumes that gas and melt

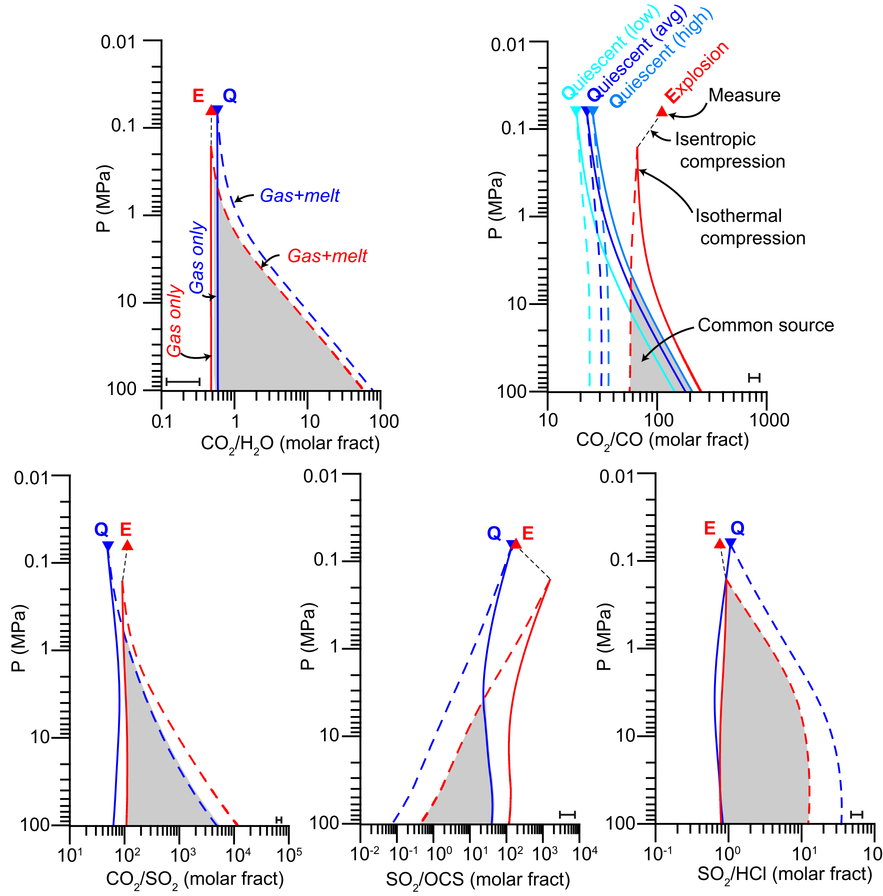

Fig. 12. Modelled evolution of the gas composition as a function of pressure at Erebus. Blue triangles represent the gas measured at the quiescent lake surface (average temperature 1022 °C) and red triangles represent the gas composition of the explosion at 9:09 referenced by an arrow on Fig. 10. Dashed curves represent gas + melt backtrackings of a convecting column (blue curve) and a slow slug (red curve). Solid curves represent gas-only backtrackings of a stagnant column (blue curve) and a fast slug (red curve, see Supplementary Tables 3–13 for full model outputs). Black dotted lines link the measured post-burst explosive composition at 838 °C to the higher pressure, pre-burst value assumed to equilibrate at 1022 °C. Grey areas cover the overlap between the span of model outputs for quiescent and explosive degassing. Horizontal error bars represent the model uncertainties for gas + melt runs (dashed curves), and model uncertainties for gas-only runs (solid curves) are smaller than curve thickness. Errors for SO_2/HCl were calculated from model outputs at 100 MPa (Supplementary Tables 7 and 12–13) and those for the other species ratios are from Burgisser et al. [9]. The three blue triangles on the CO_2/CO graph represent low, average and high temperatures of Fig. 10, respectively and the six associated blue curves are backtrackings of the respective CO_2/CO ratios. For clarity, the low- and high-temperature cases have been omitted from the other graphs because they are similar to (i.e., plot at a line thickness of) the average temperature curves. (For interpretation of the references to colour in this figure legend, the reader is referred to the web version of this article.)

rise together in closed system to reach a high, arbitrary porosity at the surface (‘gas+melt’ run). This represents a slug moving slowly enough to maintain chemical equilibrium with a thin melt shell. The other end-member considers a fast-rising slug that moves independently from the melt (‘gas-only’ run). Both gas-only scenarios (stagnant magma column and fast slug) are calculated by first recompressing the gas alone and then use the obtained species fugacities to determine melt volatile content. Thus, in the case of a fast slug, only the melt volatile composition at the starting pressure has a physical meaning as the slug then rises without interacting with the surrounding melt. However, melt volatile compositions are given at all pressures because the starting point is unknown.

Previous work on gas data from the 2005–2006 field season at Erebus also involved recompression runs, but without chlorinated species [9]. It is thus important to quantify the changes in model outputs introduced by the addition of Cl species. Runs with and without Cl-bearing species yield similar evolutions of gas and melt volatile chemistry with pressure. More precisely, relative changes are <10% for the molar ratios in the gas phase (CO_2/H_2O, CO_2/CO, CO_2/SO_2, and SO_2/OCS) and are <25% for the dissolved species (CO_2, H_2O, H_2, and S). These changes are of the same order as model uncertainties. Thus the inclusion of Cl-bearing species in recompression runs has mostly an effect through mass balance and does not significantly change the redox balance to which most other species are sensitive. This is mostly due to the small amounts of Cl-bearing species in the gas phase at Erebus, as larger Cl amounts would be able to affect the partition of the other volatiles. Chlorinated species thus play a role similar to OCS, which acts as an additional constraint on the system but does not control the evolution of the other species as pressure changes.

Fig. 12 presents the pressure evolutions of the three quiescent gas compositions and the one explosive gas composition (full model outputs are given in Supplementary Tables 3–13). At the scale of the graphs, the difference between low, average, and high quiescent temperatures is only clearly visible for the CO_2/CO ratio. All ratios have distinct compression paths for the quiescent regime and the explosion. Overall, these paths are similar to those presented in Burgisser et al. [9], which started from average gas compositions of the quiescent degassing and 18 explosions that occurred in 2005/2006. The common source areas defined by the overlap between ‘gas-only’ and ‘gas + melt’ runs for passive and explosive degassing extend from the highest pressure (100 MPa) to a few MPa. These common areas are also similar to those found for the 2005/2006 field season [9].

The ratio chosen to best represent the chlorinated species is the SO_2/HCl ratio for two reasons. First and in contrast with the input Cl-bearing ratio, CO_2/HCl, it presents quite distinct recompression

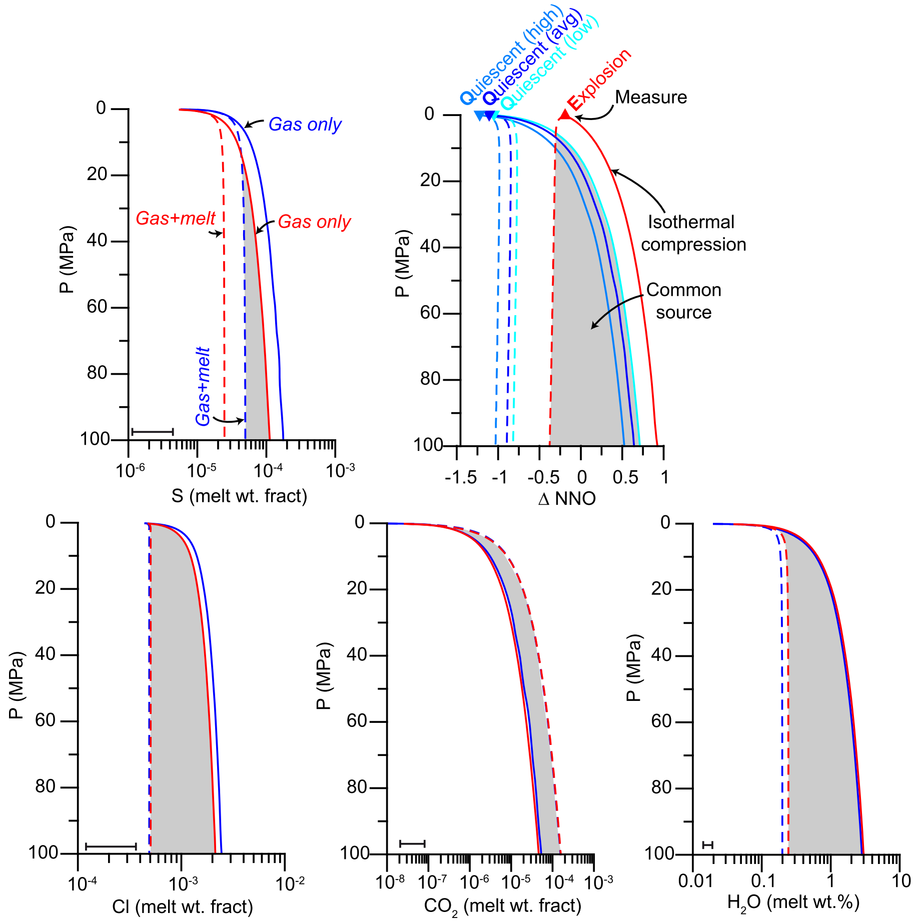

Fig. 13. Modelled evolution of melt volatile content and redox state (referenced to the Ni–NiO solid buffer) as a function of pressure at Erebus. Dashed curves represent gas + melt backtrackings of a convecting column (blue curve) and a slow slug (red curve). Solid curves represent gas-only backtrackings of a stagnant column (blue curve) and a fast slug (red curve, see Supplementary Tables 3–13 for full model outputs). Grey areas cover the overlap between the span of model outputs for quiescent and explosive degassing where uncertainties are small enough to discriminate between curves. Horizontal error bars represent model uncertainties due to solubility law fitting. Errors for Cl were calculated from model outputs at 100 MPa (Supplementary Tables 7 and 12–13) and those for the other species are from Burgisser et al. [9]. The three blue triangles on the redox graph represent low, average and high temperatures of Fig. 10, respectively and the six associated blue curves are backtrackings of the respective redox conditions. The red triangle represents the redox state of the explosion at 9:09 referenced by an arrow on Fig. 10. For clarity, the low and high temperature cases have been omitted from the other graphs because they are similar to (i.e., plot at a line thickness of) the average temperature curves. (For interpretation of the references to colour in this figure legend, the reader is referred to the web version of this article.)

paths between explosive and quiescent initial compositions and hence a more restricted common area. Second, SO_2 and HCl are among the two most commonly measured species in volcanic plumes [38] and their covariation with pressure is thus of interest. Fig. 12 shows that this new ratio varies by at least an order of magnitude for ‘gas + melt’ runs when the pressure changes from atmospheric to 100 MPa and that it varies by less than a factor of two in ‘gas-only’ runs over the same pressure range. The overlap between quiescence and explosion is comparable to those of the other ratios in the sense that it extends from 0.2 to >100 MPa.

The evolution of melt volatile content is clearest when plotted against a linear axis of pressure instead of a logarithmic one (Fig. 13). In general, the change in melt volatile content from 100 to 10 MPa is much smaller than that from 10 MPa to atmospheric pressure. Overall, these runs define common areas between quiescent and explosive behaviour that are similar to those stemming from gas composition (Fig. 12). Model uncertainties are low enough to distinguish between ‘gas-only’ and ‘gas + melt’ runs for Cl and H_2O. This is not the case for S and CO_2. Leaving these two species aside, the model runs shown in Fig. 13 suggest that low values of melt H_2O content (~0.2 wt.%) and Cl melt content (~0.05 wt.%) are typical for ‘gas + melt’ runs and that high values of melt H_2O content (~3 wt.%) and Cl melt content (~0.2 wt.%) are typical for ‘gas-only’ runs. Matrix glass and melt inclusions have Cl contents (Fig. 9b) that overlap those predicted for both scenarios, but they have H_2O contents (<0.2 wt.%) that favour ‘gas + melt’ scenarios.

4. Discussion

The partitioning of chlorides between a silicate melt and a fluid phase in equilibrium does not follow a Nernst distribution law, except at low Cl concentrations [56,1,50,68] and references cited therein). Despite data scattering and large uncertainties, our data provide evidence for the equilibrium of Cl among three phases: the silicate melt, the vapour phase, and a hydro-saline liquid (Figs. 3, 4, 7 and 8). The precisions of both our fluid compositions and the location of the immiscibility field in the H_2O–NaCl system at 1000 °C are not sufficient to conduct a rigorous modelling of Cl behaviour in high-temperature phonolites. The subset we selected to model the HCl–H_2O fluid, albeit restricted to alkaline phonolites <100 MPa, is appropriate for the Erebus magma system. The vertical extent of the light grey areas in Fig. 8 shows the likely range of melt Cl content at Erebus from melt inclusions [41] and matrix glass [9]. The horizontal range shows $^{eq}C^{f}_{NaCl}$ in the gas calculated from the quiescent maximum and minimum HCl/H_2O ratio (assuming that the quantities of HCl and NaCl are equivalent). Fig. 8B shows that the natural ranges partially overlap the experimental ones and that the assumption that Erebus degassing is not affected by immiscibility is most likely valid. To characterise such a complex system more fully than in the present work, one could recover and analyse the fluid phase, or assess precisely the fluid/melt exchanges of alkalis and Fe by carrying out experiments under the same conditions as ours but with a much larger fluid/melt ratio [69]. In the meantime, consideration of other trends of Cl distribution between the phonolitic melt and the fluid (understood as vapour + brine) is needed to explain our results for partitioning coefficients (Fig. 6).

4.1. Cl partitioning behaviour in other phonolitic melts

A few other studies have been published concerning Cl solubility and partitioning between a phonolitic melt and a fluid phase. Signorelli and Carroll [54] performed experiments spanning a wide range of pressures (Fig. 6) while others investigated variation in temperature [13] and the effects of other volatiles in the melts [13], with fluorine; [68], with sulphur).

Chevychelov et al. [13] studied chlorine and fluorine partitioning between a synthetic K-rich phonolitic melt (corresponding to the phonolite erupted at Vesuvius in the 79 A.D. eruption) and a H_2O–Cl–F fluid at 200 MPa. The two sets of data they provide unfortunately suffer from an internal inconsistency with respect to the redox conditions, which is due to the different devices used for high-temperature experiments (~NNO+3.5) and for low-temperature experiments (~NNO). Nevertheless, they suggest that the concentration of chlorine in the melt may increase with increasing fluorine in the system and that the unmixing of the fluid phase may begin at pressures as high as 200 MPa, at both 850 and 1000 °C. They do not observe any clear effect of temperature or oxygen fugacity on the partitioning of chlorine.

Webster et al. [68] performed studies of solubility and partitioning of Cl between a K-phonolitic melt and an S- and Cl-bearing hydrous fluid at the relatively oxidising conditions of NNO+1. They observed that the concentration of Cl in the melt decreases with increasing S in the system and they confirm a positive dependence with temperature previously found by Webster and De Vivo [66], which is, in part, a secondary effect of the high Fe and Ca content in the highest-temperature experiments.

These two previous studies involved K-phonolitic peralkaline melts and only Signorelli and Carroll [54] performed experiments using a Na-phonolite from Montaña Blanca (Tenerife) that approaches the Erebus composition. Signorelli and Carroll [54] found that chlorine solubility in phonolitic melts saturated with vapour + brine follows a negative dependence with pressure from 250 to 50 MPa and they derived partition coefficients of Cl between the two phases in a way similar to our approach. They most likely did not find the positive dependence that our data show (Fig. 6) because of the low pressures at which this trend occurs.

The available data from these three studies do not allow us to carry out an in-depth comparison, but they provide interesting insights. Fig. 14 shows the Cl concentration in the melt as a function of Cl concentration in the coexisting fluid phase for experiments at 200 MPa, the sole common pressure that all the experimental studies covered. The comparison between the data of Webster et al. [68] and those of Chevychelov et al. [13] at 1000 °C suggests that more reduced conditions may favour the dissolution of chlorine in the melt. A previous study on peralkaline magmas [15] already mentioned a similar behaviour with higher Cl solubilities at NNO−2 than those measured at NNO+2. These observations contrast with those of Alletti et al. [1], who performed several experiments on Cl partitioning between a basaltic melt and a fluid phase and noted a small increase of $D_{Cl}^{f/m}$ in the more oxidising experiments (i.e. higher dissolution of chlorine in the melt). The comparison between their data with those of Stelling et al. [56] obtained at slightly more reduced conditions confirms the possible dependence of Cl dissolution behaviour with f_{O2}, but with a different underlying control to that we propose for more evolved melts. Many variables can also explain this apparent discrepancy, such as the very different melt composition and the associated dissimilarities in melt structure, or the temperature of the experiments. Effects of this last variable can be seen in Fig. 14, which compares data from Webster et al. [68] and Signorelli and Carroll [54] at similar oxygen fugacities. Webster et al. [68] proposed that the effects of temperature and f_{O2} may compensate each other and their result at T ~850 °C for an F-poor experiment is in good agreement with the experiment of Signorelli and Carroll [54] for a K-phonolitic melt at similar conditions (Fig. 14). Keeping in mind that the discrepancy between our data and those of Webster et al. [68] can be explained by the facts that their experiments were mainly conducted in Cl-saturated and H_2O-poor melts, while our experiments have been performed in water-rich conditions and that melt H_2O content and Cl solubility are strictly related, overall our data support the previously inferred effects of temperature and oxygen fugacity on Cl partitioning.

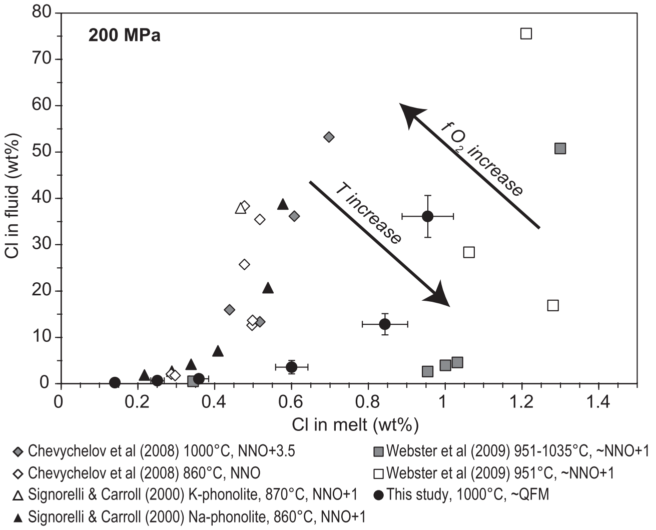

Fig. 14. Distribution of Cl content in the fluid versus Cl content in the melt for several studies on phonolitic melts. The comparison suggests a negative correlation between $D_{Cl}^{f/m}$ and temperature and an increase of $D_{Cl}^{f/m}$ with more oxidized conditions. Data sources are listed in the legend and Cl fluid content for our experiments are ${}^{eq\text{-}HCl}C_{Cl}^{f}$ (see text for more explanations).

4.2. Interpreting the gas signature at Erebus

The chemical composition and flux of the gas plume at Erebus fluctuates cyclically [40,5,33,44,45]. These quasi-periodic variations are remarkably in phase with changes in heat loss at the surface of the lake and changes of the surface velocity of the magma [40]. In a study of thermal imagery of the lake acquired annually from 2004 to 2011, Peters et al. [44] and Peters et al. [45] showed the cyclic behaviour to be a persistent feature with period varying from 5 to 18 min. Here, we have used the gas composition data to compute time-series changes of equilibrium gas temperatures. Our results suggest that during one day in late 2010 temperature fluctuated with a period of 7–9 min for an hour or so followed by more irregular variations with a dominant 20-min period. These fluctuations are very likely to have the same dynamical origin as the oscillations in heat loss and lake surface motion recognised in 2004–2011.

Our data show that the average quiescent temperature of the lake on 15 December 2010 is 1026 °C with a low-temperature range of ∼1000 °C and a high of ∼1050 °C. This is significantly lower (i.e. it exceeds the 5 °C model accuracy) than the quiescent lake temperature in late 2005 (1069–1084 °C with an average around 1080 °C, [9]) and it is closer to older (980–1030 °C, [27,19]) and more recent (950 ± 25 °C, [34]) phonolite lava temperature estimates derived from petrological evidence. Taking into account that temperature gradients are expected in a convecting lake and conduit (possibly ranging at Erebus from 30 to 60 °C according to the numerical simulations of [31]) and the yearly variations of ∼60 °C given by gas modelling, such a span of temperatures for the lava lake and the shallow plumbing system is not surprising.

Our thermodynamic modelling takes into consideration only HCl and Cl_2 below 100 MPa, neglecting the NaCl-rich fluid phase that dominates at higher pressures and/or total Cl content. This is likely valid at Erebus (Fig. 8B), but restricts model application to Cl-poor systems. We carried out recompression runs using representative quiescent and explosive gases from late 2010 at Erebus. The common source areas defined by the overlap between 'gas-only' and 'gas + melt' runs for quiescent and explosive degassing extend from the highest pressure (100 MPa) to a few MPa. These common areas are similar to those found in the 2005/2006 field season [9]. Only the 'gas + melt' runs predict melt water contents compatible with and those measured in matrix glass and melt inclusions. Since the compositional evolutions of these 'gas + melt' runs are parallel >10 MPa and within error for most variables (Figs. 12 and 13), a narrowing of the common areas between quiescent and explosive behaviour is not possible at this stage. Leaving aside explosions because their rapid kinetics is unlikely to affect volatiles in isolated melt inclusions, this result nevertheless suggests that the passive degassing is caused by a slowly convecting column. This interpretation is consistent with our previous modelling effort [9] and with the pressure-temperature trajectories of single crystals (Moussallam et al. [36] in review).

Although the partitioning between gaseous and melt-dissolved Cl-bearing species is sensitive to the redox state of the system (Fig. 14), the redox state is not sensitive to the presence or absence of chlorinated species at such low pressures. The implication for volcanic gas modelling is that adding Cl to the O–H–S–C system has only a minor effect on model outputs (<10% for the molar ratios in the gas phase and <25% for the dissolved species). The measurement of HCl in the gas plume, however, provides further evidence that the measured gas composition at Erebus corresponds to high-temperature equilibrium (see the discussion on the absence of measurable H_2S in the plume in [9]). Conversely, the inclusion of Cl-bearing species in modelling allows for the study of the evolution of SO_2/HCl, an often-measured chemical ratio in volcanic plumes (e.g., [21,39,20,10,14]).

Fig. 15 shows the range of SO_2/HCl values measured in volcanic plumes from seven well-studied volcanoes. In all cases, systematic SO_2/HCl variations correlate with eruptive intensity. Although compositional effects play an important role (e.g., basaltic melts can accommodate more Cl than more silicic ones, [56]), our treatment of Cl solubility in phonolites allows us to make some first-order observations. Our modelling suggests that SO_2/HCl varies little with pressure when degassing involves gas and melt but that strong variations occur at low (<5 MPa) pressure in 'gas-only' runs (Fig. 12). These variations can span up to one order of magnitude, which is also the level that measurement ranges reach (Fig. 15). In agreement with considerations presented by Shinhoara (2009), this suggests that very shallow decoupling of gas and magma is a viable mechanism to explain strong variations of SO_2/HCl in volcanic plumes. Our modelling, although still based on crude physical templates of magma ascent and restricted to low Cl content, provides a detailed treatment of the buffering capacity of the gas phase. It demonstrates the fundamental link between variations in gas chemistry and eruptive regimes.

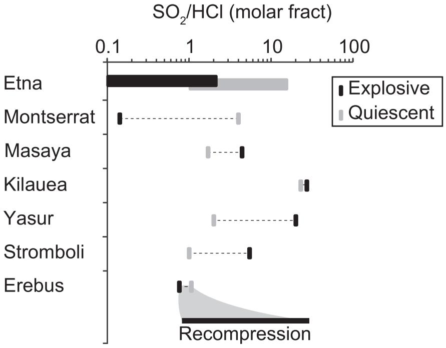

Fig. 15. Molar ratios of SO_2/HCl in volcanic gases. Although ranges (dashed lines) of gas composition have been measured at the volcanoes listed along the vertical axis, extreme measures often correspond to either explosive (black bars) or quiescent (grey bars) degassing. Erebus gas data are linked by a grey area to a horizontal black line that covers the range of SO_2/HCl values given by the recompression of the gases (larger values are achieved by gas + melt degassing). Data are taken from Edmonds et al. [21], Duffel et al. [18], Oppenheimer et al. [39], Edmonds and Gerlach [20], Burton et al. [10], Aiuppa [2], and Christopher et al. [14].

5. Conclusions

We conducted a series of high-pressure, high-temperature experiments on phonolite from Erebus volcano so as to quantify the solubility of chorine in the presence of water. We investigated the pressure range from 10 to 250 MPa at a constant temperature of 1000 °C and redox conditions close to the QFM buffer. At each investigated pressure, we used several experimental charges loaded with various amounts of Cl so as to obtain a range of Cl concentrations. An immiscibility gap in the fluid phase affects some of our runs. As a result, only a partial view of the system behaviour was gained by determining the partition coefficient of Cl, $D_{Cl}^{f/m}$, for the runs with the lowest fluid and melt Cl contents. The resulting $D_{Cl}^{f/m}$ decreases from 6.0 to 1.7 when the pressure decreases from 250 to 100 MPa, and increases back to 10.2 when the pressure decreases to 10 MPa. The increase at low pressure was not hitherto recognised in phonolite melts (e.g., [54]) because of the lack of low pressure data.

Only one of our 48 experimental samples shows coexistence of low-density vapour and high-density brine while 35 samples are unambiguously in the vapour field. Large uncertainties in the phase diagram H_2O–NaCl at the *P*–*T* considered and large uncertainties in our fluid phase composition preclude us from assigning reliable phase behaviour to the 12 remaining samples. We used this interpretative framework and estimates of the Cl content of the Erebus system to select the vapour-dominated subset of our dataset. Assuming that chlorine was present in this subset as HCl, we related Cl melt content to HCl fugacity at low pressures (atmospheric to 100 MPa). We incorporated the new HCl solubility law into a thermodynamical model [9] so that it calculates the C–O–H–S–Cl equilibrium compositions of volatiles dissolved into a phonolitic melt and a coexisting fluid phase at magmatic temperatures. We implemented a new method of solution to find equilibrium gas temperature at a given pressure that takes molar ratios of gas species as input instead of gas fugacities.

We modelled a day-long time series of volcanic gas composition measurements obtained from open-path FTIR absorption spectra collected at Erebus on 15 December 2010. The measured molar ratios of CO_2/H_2O, CO_2/CO, CO_2/SO_2, SO_2/OCS, and CO_2/HCl were entered into the thermodynamical model to calculate the evolution of gas temperature over ~7.5 h. Analysis of this time series shows that visually recorded explosions of metre-sized gas bubbles in the lake correspond to troughs in the equilibrium temperature time series. The temperature fluctuates cyclically with a period of 7–9 min at the beginning of the day followed by more irregular cycles with a dominant 20-min period. Overall, the average quiescent lake temperature of the lake in late 2010 was 1026 ± 25 °C. This is lower that the quiescent lake temperature in late 2005 (1077 ± 8 °C, [9]. We interpret such a range of values to reflect the temperature gradients expected in a convecting lake and associated shallow plumbing system [31].

We carried out recompression runs of the passive and explosive gas compositions, following the method outlined in Burgisser et al. [9]. The domain of compositions and pressures from which both passive and explosive gases may originate extends from 100 MPa to a few MPa, which is similar to that found for gas composition data from late 2005 using a Cl-free version of the model [9]. This is not surprising since adding Cl to the O–H–S–C system has only a minor impact on model outputs (<10% change in molar ratios in the gas phase and <25% change in dissolved species). One interest of including Cl-bearing species in the modelling is that it allows for the study of the evolution of SO_2/HCl, an often-measured chemical ratio in volcanic plumes. Our runs show that when the pressure changes from 100 MPa to atmospheric, this ratio varies by at least an order of magnitude for coupled, gas-and-melt runs and by less than a factor of two for decoupled, gas-only runs. Changes of SO_2/HCl in volcanic plumes can thus be caused by shallow changes in gas/melt separation regime.

Acknowledgements

Thoughtful comments and reviews by R. Botcharnikov, D. Pyle, and J. Webster are greatly appreciated. This research was partially supported by grants ANT-0838817 from the Office of Polar Programs (National Science Foundation), and 202844 from the European Research Council (under the European FP7).

Appendix A. Supplementary data

Supplementary data associated with this article can be found, in the online version, at http://dx.doi.org/10.1016/j.grj.2014.09.003.

References

[1] Alletti M, Baker DR, Scaillet B, Aiuppa A, Moretti R, Ottolini L. Chlorine partitioning between a basaltic melt and H2O-CO2 fluids at Mount Etna. Chem Geol 2009;263(1–4):37–50.

[2] Aiuppa A. Degassing of halogens from basaltic volcanism: Insights from volcanic gas observations. Chem Geol 2009;263(1–4):99–109.

[3] Anderko A, Pitzer KS. Equation-of-state representation of phase equilibria and volumetric, properties of the system NaCl-H2O above 573 K. Geochim Cosmochim Acta 1993;57:1657–80.

[4] Bodnar RJ, Burnham CW, Sterner SM. Synthetic fluid inclusions in natural quartz. III. Determination of phase equilibrium properties in the system H2O-NaCl to 1000°C and 1500 bars. Geochim Cosmochim Acta 1985;49:1861–73.

[5] Boichu M, Oppenheimer C, Tsanev V, Kyle PR. High temporal resolution SO2 flux measurements at Erebus volcano, Antarctica. J Volcanol Geoth Res 2010;190(3–4):325–36.

[6] Botcharnikov RE, Behrens H, Holtz F, Koepke J, Sato H. Sulfur and chlorine solubility in Mt. Unzen rhyodacite melt at 850 & #xB0;C and 200 MPa. Chem Geol 2004;213:207–25.

[7] Burgisser A, Scaillet B. Redox evolution of a degassing magma rising to the surface. Nature 2007;445(7124):194–7.

[8] Burgisser A, Scaillet B, Harshvardhan. Chemical patterns of erupting silicic magmas and their influence on the amount of degassing during ascent. J Geophys Res Solid Earth 2008;113(B12). http://dx.doi.org/10.1029/2008JB005680.

[9] Burgisser A, Oppenheimer C, Alletti M, Kyle PR, Scaillet B, Carroll MR. Backward tracking of gas chemistry measurements at Erebus volcano. Geochem Geophys Geosyst 2012;13. http://dx.doi.org/10.1029/2012GC004243.

[10] Burton M, Allard P, Muré F, La Spina A. Magmatic gas composition reveals the source depth of slug-driven Strombolian explosive activity. Science 2007;317:227–30.

[11] Carroll M, Holloway JR. Volatiles in magma. Mineral Soc Am Rev Mineral 1994;30:517.

[12] Carroll MR, Blank JG. The solubility of H2O in phonolitic melts. Am Mineral 1997;82(5–6):549–56.

[13] Chevychelov VY, Botcharnikov RE, Holtz F. Partitioning of Cl and F between fluid and hydrous phonolitic melt of Mt. Vesuvius at similar to 850–1000 degrees C and 200 MPa. Chem Geol 2008;256(3–4):172–84.

[14] Christopher T, Edmonds M, Humphreys MCS, Herd RA. Volcanic gas emissions from Soufriere Hills Volcano, Montserrat 1995–2009, with implications for mafic magma supply and degassing. Geophys Res Lett 2010;37. http://dx.doi.org/10.1029/2009GL041325.

[15] Di Carlo I, Rotolo SG, Scaillet B, Buccheri V, Pichavant M. Phase equilibrium constraints on pre-eruptive conditions of recent felsic explosive volcanism at Pantelleria Island, Italy. J Petrol 2007;51:2245–76.

[16] Di Carlo I, Pichavant M, Rotolo SG, Scaillet B. Experimental crystallization of a high-K arc basalt: the golden pumice, Stromboli volcano (Italy). J Petrol 2006;47:1317–43.

[17] Driesner T, Heinrich CA. The system H2O-NaCl. Part I: Correlation formulae for phase relations in temperature-pressure-composition space from 0 to 1000 degrees C, 0 to 5000 bar, and 0 to 1 X-NaCl. Geochim Cosmochim Acta 2007;71(20):4880–901.

[18] Duffel HJ, Oppenheimer C, Pyle DM, Galle B, McGonigle AJS, Burton MR. Changes in gas composition prior to a minor explosive eruption at Masaya volcano, Nicaragua. J Volcanol Geoth Res 2003;126:327–39.

[19] Dunbar NW, K.V. Cashman, Dupre R. Crystallization processes of anorthoclase phenocrysts in the Mount Erebus magmatic system: evidence from crystal composition, crystal size distributions and volatile contents of melt inclusions. In: Kyle PR, editor. Volcanological and environmental studies of Mount Erebus, Antarctica, vol. 66. Washington, D.C.: Antarct. Res. Ser., AGU; 1994. p. 129–46.

[20] Edmonds M, Gerlach TM. Vapor segregation and loss in basaltic melts. Geology 2007;35(8):751–4.

[21] Edmonds M, Pyle D, Oppenheimer C. HCl emissions at Soufriere Hills Volcano, Montserrat, West Indies, during a second phase of dome building: November 1999 to October 2000. Bull Volcanol 2002;64(1):21–30.

[22] Frank MR, Candela PA, Piccoli PM. Alkali exchange equilibria between a silicate melt and coexisting magmatic volatile phase: An experimental study at 800°C and 100 MPa. Geochim Cosmochim Acta 2003;67:1415–27. http://dx.doi.org/10.1016/S0016-7037(02)01181-X.

[23] Gardner, J. E., A. Burgisser, M. Hort, and M. Rutherford (2006), Experimental and model constraints on degassing of magma during ascent and eruption, Neogene-Quarternary Continental Margin Volcanism: A Perspective from Mexico, vol. 402, p. 99–113.

[24] Holloway JR. Igneous fluids. Rev Mineral 1987;17:211–33.

[25] Iacono-Marziano G, Schmidt BC, Dolfi D. Equilibrium and disequilibrium degassing of a phonolitic melt (Vesuvius AD 79 "white pumice") simulated by decompression experiments. J Volcanol Geoth Res 2007;161(3):151–64.

[26] Kelly PJ, Kyle PR, Dunbar NW, Sims KWW. Geochemistry and mineralogy of the phonolite lava lake, Erebus volcano, Antarctica: 1972–2004 and comparison with older lavas. J Volcanol Geoth Res 2008;177(3):589–605.

[27] Kyle PR. Mineralogy and glass chemistry of recent volcanic ejecta from Mount Erebus, Ross-Island, Antarctica. NZ J Geol Geophys 1977;20(6):1123–46.

[28] Larsen JF, Gardner JE. Experimental study of water degassing from phonolite melts: implications for volatile oversaturation during magmatic ascent. J Volcanol Geoth Res 2004;134:109–24.

[29] Liebscher A. Aqueous fluids at elevated pressure and temperature. Geofluids 2010;10:3–19. http://dx.doi.org/10.1111/j.1468-8123.2010.00293.x.

[30] Lowenstern JB. A review of the contrasting behavior of two magmatic volatiles: chlorine and carbon dioxide. J Geochem Explor 2000;69–70:287–90.

[31] Molina I, Burgisser A, Oppenheimer C. Numerical simulations of convection in crystal-bearing magmas: a case study of the magmatic system at Erebus, Antarctica. J Geophys Res 2012;117:B07209. http://dx.doi.org/10.1029/2011JB008760.

[32] Morizet Y, Brooker RA, Kohn SC. CO2 in haplo-phonolite Melt: Solubility, speciation and carbonate complexation. Geochim Cosmochim Acta 2002;66(10):1809–20.

[33] Moussallam Y, Oppenheimer C, Aiuppa A, Giudice G, Moussallam M, Kyle P. Hydrogen emissions from Erebus volcano, Antarctica. Bull Volcanol 2012;74(9):2109–20.

[34] Moussallam Y, Oppenheimer C, Scaillet B, Kyle PR. Experimental Phase-equilibrium Constraints on the Phonolite Magmatic System of Erebus Volcano, Antarctica. J Petrol 2013;54(7):1285–307.

[35] Moussallam Y, Oppenheimer C, Scaillet B, Gaillard F, Kyle P, Peters N, Hartley M, Berlo K, Donovan A. Tracking the changing oxidation state of Erebus magmas, from mantle to surface, driven by magma ascent and degassing. Earth Planet Sci Lett 2014;393:200–9. http://dx.doi.org/10.1016/j.epsl.2014.02.055.

[36] Moussallam Y, Oppenheimer C, Scaillet B, Buisman I, Kimball C, Dunbar N, Burgisser A, Schipper CI, Andújar J, Kyle P. Riding the conduit elevator at Erebus volcano: magma motion and speed recorded by anorthoclase megacrystals. Earth Planet Sci Lett 2014. in review.

[37] Oppenheimer C, Kyle PR. Probing the magma plumbing of Erebus volcano, Antarctica, by open-path FTIR spectroscopy of gas emissions. J Volcanol Geoth Res 2008;177(3):743–54.

[38] Oppenheimer C, Fischer TP, Scaillet B. Volcanic degassing: Process and impact 2nd ed. In: Holland HD, Turekian KK, editor. Treatise on Geochemistry, vol. 4, Elsevier; 2014. p. 111–179, doi: 10.1016/B978-0-08-095975-7.00304-1.

[39] Oppenheimer C, Bani P, Calkins JA, Burton MR, Sawyer GM. Rapid FTIR sensing of volcanic gases released by Strombolian explosions at Yasur volcano, Vanuatu. Appl Phys B Lasers Opt 2006;85(2–3):453–60.

[40] Oppenheimer C, Lomakina AS, Kyle PR, Kingsbury NG, Boichu M. Pulsatory magma supply to a phonolite lava lake. Earth Planet Sci Lett 2009;284(3–4):392–8.

[41] Oppenheimer C, Moretti R, Kyle PR, Eschenbacher A, Lowenstern JB, Hervig RL, Dunbar NW. Mantle to surface degassing of alkalic magmas at Erebus volcano, Antarctica. Earth Planet Sci Lett 2011;306(3–4):261–71.

[42] Papale P, Moretti R, Barbato D. The compositional dependence of the saturation surface of H2O+CO2 fluids in silicate melts. Chem Geol 2006;229(1–3):78–95.

[43] Peretyazhko IS. Inclusions of magmatic fluids: P-V–T–X properties of aqueous salt solutions of various types and petrological implications. Petrology 2009;17:178–201.

[44] Peters N, Oppenheimer C, Kyle P, Kingsbury N. Decadal persistence of cycles in lava lake motion at Erebus volcano, Antarctica. Earth Planet Sci Lett 2014;395:1–12. http://dx.doi.org/10.1016/j.epsl.2014.03.032.

[45] Peters N, Oppenheimer C, Killingsworth DR, Frechette J, Kyle P. Correlation of cycles in lava lake motion and degassing at Erebus volcano, Antarctica. Geochem Geophys Geosyst 2014;15. http://dx.doi.org/10.1002/2014GC005399.

[46] Reed BC. Linear least-squares fits with errors in both coordinates. Am J Phys 1989;57(7):642–6.

[47] Robie RA, Hemingway BS, Fisher JR. Thermodynamic properties of minerals and related substances at 298.15 K and 1 bar (10^5 pascals) pressure and at higher temperatures. US Geol Surv Bull 1979:1452–6.

[48] Schmidt BC, Behrens H. Water solubility in phonolite melts: Influence of melt composition and temperature. Chem Geol 2008;256(3–4):259–68.

[49] Shinohara H. Exsolution of immiscible vapor and liquid-phases from a crystallizing silicate melt - implications for chlorine and metal transport. Geochim Cosmochim Acta 1994;58(23):5215–21.

[50] Shinohara H. A missing link between volcanic degassing and experimental studies on chloride partitioning. Chem Geol 2009;263(1–4):51–9.

[51] Shinohara H, Iiyama JT, Matsuo S. Partition of chlorine compounds between silicate melt and hydrothermal solutions 1. Partition of NaCl-KCl. Geochim Cosmochim Acta 1989;53(10):2617–30.

[52] Shmulovich KI, Churakov SV. Natural fluid phases at high temperatures and low pressures. J Geochem Explor 1998;62:183–91.

[53] Shmulovich K, Henrich W, Möller P, Dulski P. Experimental determination of REE fractionation between liquid and vapour in the systems NaCl–H2O and CaCl2–H2O up to 450 °C. Contrib Miner Petrol 2002;144:257–73. http://dx.doi.org/10.1007/s00410-002-0397-y.

[54] Signorelli S, Carroll MR. Solubility and fluid-melt partitioning of Cl in hydrous phonolitic melts. Geochim Cosmochim Acta 2000;64(16):2851–62.

[55] Signorelli S, Carroll MR. Experimental study of Cl solubility in hydrous alkaline melts: constraints on the theoretical maximum amount of Cl in trachytic and phonolitic melts. Contrib Miner Petrol 2002;143(2):209–18.

[56] Stelling J, Botcharnikov RE, Beermann O, Nowak M. Solubility of H(2)O- and chlorine-bearing fluids in basaltic melt of Mount Etna at T = 1050–1250 degrees C and P = 200 MPa. Chem Geol 2008;256(3–4):102–10.

[57] Symonds RB, Reed MH. Calculation of multicomponent chemical equilibria in gas-solid-liquid systems: calculation methods, thermochemical data, and applications to studies of high-temperature volcanic gases with examples from Mount St. Helens. Am J Sci 1993;293:758–864.

[58] Taran YA, Hedenquist JW, Korzhinsky MA, Tkachenko SI, Shmulovich KI. Geochemistry of magmatic gases from Kudryavy volcano, Iturup, Kuril Islands. Geochim Cosmochim Acta 1995;59:1749–61.

[59] Taylor JR, Wall VJ, Pownceby MI. The calibration and application of accurate redox sensors. Am Mineral 1992;77(3–4):284–95.

[60] Taylor JR. An introduction to error analysis – the study of uncertainties in physical measurements. Sausalito, California: University Science Books; 1997. p. 327.

[61] Veksler IV. Liquid immiscibility and its role at the magmatic–hydrothermal transition: a summary of experimental studies. Chem Geol 2004;210:7–31.

[62] Villemant B, Boudon G. H2O and halogen (F, Cl, Br) behaviour during shallow magma degassing processes. Earth Planet Sci Lett 1999;168(3–4):271–86.

[63] Villemant B, Mouatt J, Michel A. Andesitic magma degassing investigated through H(2)O vapour-melt partitioning of halogens at Soufriere Hills Volcano, Montserrat (Lesser Antilles). Earth Planet Sci Lett 2008;269(1–2):212–29.

[64] Webster JD. Fluid-melt interactions involving Cl-rich granites: experimental study from 2 to 8 kbar. Geochim Cosmochim Acta 1992;56:659–78.

[65] Webster JD. Chloride solubility in felsic melts and the role of chloride in magmatic degassing. J Petrol 1997;38(12):1793–807.

[66] Webster JD, De Vivo B. Experimental and modeled solubilities of chlorine in aluminosilicate melts, consequences of magma evolution, and implications for exsolution of hydrous chloride melt at Mt. Somma-Vesuvius. Am Mineral 2002;87:1046–61.

[67] Webster JD, Kinzler RJ, Mathez EA. Chloride and water solubility in basalt and andesite melts and implications for magmatic degassing. Geochim Cosmochim Acta 1999;63(5):729–38.

[68] Webster JD, Sintoni MF, De Vivo B. The partitioning behavior of Cl, S, and H2O in aqueous vapor- +/− saline-liquid saturated phonolitic and trachytic melts at 200 MPa. Chem Geol 2009;263(1–4):19–36.

[69] Zajacz Z, Candela PA, Piccoli PM, Sanchez-Valle C. The partitioning of sulfur and chlorine between andesite melts and magmatic volatiles and the exchange coefficients of major cations. Geochim Cosmochim Acta 2012;89:81–101.